Many-body effects in weakly bound anion and neutral clusters: Zero electron kinetic energy spectroscopy and threshold photodetachment spectroscopy of Ar_nBr^- ($n=2-9$) and Ar_nI^- ($n=2-19$)

Ivan Yourshaw, Yuexing Zhao, and Daniel M. Neumark
Department of Chemistry, University of California, Berkeley, California 94720 and Chemical Sciences Division, Lawrence Berkeley National Laboratory, Berkeley, California 94720

(Received 19 December 1995; accepted 3 April 1996)

The anion zero electron kinetic energy (ZEKE) spectra of the van der Waals clusters $Ar_{2-3}Br^-$ and $Ar_{2-3}I^-$ have been measured, and partially discriminated threshold photodetachment (PDTP) experiments have been performed on $Ar_{4-9}Br^-$ and $Ar_{8-19}I^-$. The experiments yield size-dependent adiabatic electron affinities (EAs) and electronic state splittings of the halogen atom in the neutral clusters formed by photodetachment. These results are compared with simulated annealing calculations using model potentials for the anion and neutral clusters, making use of the neutral and anion pair potentials determined from previous work on the diatomic rare gas–halide atom complexes [Y. Zhao, I. Yourshaw, G. Reiser, C. C. Arnold, and D. M. Neumark, J. Chem. Phys. **101**, 6538 (1994)]. A simple first-order degenerate perturbation theory model [W. G. Lawrence and V. A. Apkarian, J. Chem. Phys. **101**, 1820 (1994)] of the neutral cluster potentials was found to agree well with the size-dependent splitting of the halogen $^2P_{3/2}$ state observed in the ZEKE spectra. However, the binding energies calculated from the pair potentials alone were found to be inconsistent with the experimental electron affinities, and it was necessary to include various nonadditive terms in the simulated annealing calculations to obtain reasonable agreement with experiment. Many-body induction in the anion clusters was found to be the dominant nonadditive effect. The exchange quadrupole effect—i.e., the interaction of the exchange induced electron charge distribution distortion among argon atoms with the halide charge—was also found to be important. This comparison between experiment and theory provides a sensitive probe of the importance of nonadditive effects in weakly bound clusters. © *1996 American Institute of Physics.* [S0021-9606(96)01426-2]

I. INTRODUCTION

In most studies of weakly interacting atoms or molecules, pairwise additivity of the potentials is assumed. Given pair potentials, V_{ij}, between atoms i and j, the pairwise additive approximation to the total potential of N interacting atoms is

$$V_{\text{pair}}=\sum_{i<j}^{N} V_{ij}(|\mathbf{r}_i-\mathbf{r}_j|). \tag{1}$$

Here $\mathbf{r}_i$ and $\mathbf{r}_j$ represent the positions of atoms i and j. If the atoms had closed valence shells, and if no deformation of the atomic charge distributions were induced by the interactions, then pairwise additivity would hold exactly.[1] However, if the deformation of the charge distributions due to the interatomic interactions (e.g., dispersion, induction, or exchange) is considered, the assumption of pairwise additivity breaks down.[1] This assumption can also break down if one of the atoms has an open valence shell. Then it is necessary to consider the electronic states of the open-shell atom which arise from the simultaneous presence of all the other atoms; The potential energy surfaces of these states cannot, in general, be obtained by simply adding the pair potentials in the sense of Eq. (1). In either case it is necessary to extend Eq. (1) to include nonadditive, or many-body, effects:

$$\begin{aligned} V_{\text{many-body}} &= V_{\text{pair}}+V_{\text{nonadd}} \\ &= V_{\text{pair}}+\sum_{i<j<k}^{N} V_{ijk}(\mathbf{r}_i,\mathbf{r}_j,\mathbf{r}_k)+\cdots \\ &\quad +\sum_{i<j<k\cdots z}^{N} V_{ijk\cdots z}(\mathbf{r}_i,\mathbf{r}_j,\mathbf{r}_k,\cdots,\mathbf{r}_z). \end{aligned} \tag{2}$$

Nonadditive effects are believed to play a significant role in determining the properties of bulk matter. For example, the binding energies of rare gas solids (Ne, Ar, Kr and Xe) measured experimentally are about 7–10 % smaller than the binding energies calculated from accurate pair potentials.[2] However, there has been some controversy about the precise nature of the nonadditive effects involved.[2,3] Furthermore, it is in general difficult to extract detailed information about nonadditive effects from measurements of bulk properties.[3]

Cluster studies represent an alternative approach to learn about nonadditive effects. By probing the spectroscopy and/or energetics of a cluster as a function of its size, and comparing the results with predictions based on additive forces alone, one can obtain considerable insight into the various nonadditive components of the interaction potential.[3] To this end, we present in this article the anion zero electron kinetic energy (ZEKE) spectra of the $Ar_{2-3}Br^-$ and $Ar_{2-7}I^-$ van der Waals clusters and partially discriminated threshold

photodetachment (PDTP) spectra of $Ar_{4-9}Br^-$ and $Ar_{8-19}I^-$. We also present the results of calculations with model potentials involving various nonadditive terms, in an effort to understand the experimentally observed electron affinities (EAs) and electronic structure. Our results probe nonadditive effects in both the cluster anion and the open-shell neutral cluster resulting from photodetachment. This work is an extension of our previous ZEKE study of the diatomic rare gas–halide atom complexes[4] and previous ZEKE work on the I^-CO_2 complex.[5]

In order to extract information on many-body effects from experimental studies of clusters, the pair potentials must be known more accurately than the magnitude of the many-body effect. Furthermore, the experiment must provide information about the ''true'' potential that can be compared with the results of calculations with model additive and nonadditive potentials. This information may consist of spectroscopically measured vibrational frequencies, rotational constants, etc. In this case, accurate dynamical calculations are needed to extract this information from the model potentials for comparison with experiment. Alternatively, some experiments allow a more direct measurement of the cluster binding energies, in which case comparison with model potentials is much more straightforward.

Nonadditive effects can affect the rotational, vibrational, and electronic spectroscopy of a cluster. Much of the recent interest in this field has focused on high resolution spectroscopy of van der Waals clusters. For example, pure rotation spectra of Ne_2Kr and Ne_2Xe have been observed using Fourier transform microwave spectroscopy.[6] The structural information and nuclear hyperfine coupling constants determined from these spectra show evidence of nonadditivity. There have also been a number of near and far infrared studies of molecular chromophores in rare gas clusters.[3,7,8] In many cases it is difficult to extract meaningful information about many-body forces from spectroscopic studies because the intermolecular pair potentials are often not well enough characterized, in that the uncertainty in the pair potentials is comparable to the magnitude of the many-body effects. There has, however, been recent experimental and theoretical progress in determining intermolecular pair potentials accurately enough to learn about three-body interactions in the Ar_2HCl [Refs. 3, 8, 9, and 10(a)] Ar_2HF [Refs. 7, 9, and 10(c)], and Ar_2DCl [Refs. 3 and 10(b)] systems. In work more closely related to the results presented here, the electronic spectroscopy of $Ar_{1-4}Hg$ clusters has been studied with multiphoton ionization,[11] and Ar_nBa clusters have been studied by laser induced fluorescence.[12] Only the $Ar_{1-4}Hg$ study was mass-selective. From this work, progress has been made in identifying ''nonadditive'' effects in the excited electronic state of these clusters with open-shell chromophores.[11,12]

It is challenging to extract information on nonadditive effects from direct spectroscopic measurements such as those mentioned above. Even when mass selectivity can be obtained, nontrivial dynamical calculations are needed to extract the vibrational and rotational structure information from a many-body model potential in order to compare it with the experimental spectrum. It is desirable, therefore, to measure experimentally the binding energies (BEs) of clusters, because BEs can be readily obtained from many-body model potentials by simple methods. Moreover, there is generally an intuitive connection between a particular nonadditive term and the cluster binding energy, in the sense that one can usually predict by inspection if the binding energy will increase or decrease when a given many-body term is added to a model potential. However, in most cases, BEs of clusters cannot be directly obtained from experimental spectra. Exceptions include the pump–probe experiments of Janda and co-workers on $Ar_{1-3}Cl_2$ [Ref. 13(a)] and $HeBr_2$ [Ref. 13(b)] and the stimulated emission pumping experiments on the carbazole–Ar system by Leutwyler and co-workers.[14]

Anion photoelectron spectroscopy (PES) of clusters has proved useful in providing more direct information about the relative binding energies of anion and neutral clusters. It also has the advantage of mass selectivity. Examples include the work of Markovich *et al.* on $X^-(H_2O)_n$ ($X^-=Cl^-$, Br^-, and I^-),[15] Bowen and co-workers on O^-Ar_n,[16] and Arnold *et al.* on $X^-(CO_2)_n$ and $X^-(N_2O)_n$.[17] The theoretical calculations of Berkowitz and co-workers[18] in conjunction with the PES spectra of Markovich *et al.*[15] have demonstrated the importance of nonadditive inductive effects in $Br^-(H_2O)_n$ clusters.

However, there are two problems with trying to extract information on nonadditive forces from these studies. First, the pair potentials for the relevant neutral and ionic species are not in general known very accurately; this is particularly true for clusters involving molecular solvents. Second, the resolution of conventional anion PES is typically in the range of 80 cm^{-1} (Ref. 17) to 400 cm^{-1} (Ref. 15), depending on the type of energy analyzer used. Because of this limited resolution, anion PES experiments can only be sensitive to the largest nonadditive effects, such as inductive effects in the anion clusters.

The anion ZEKE technique used in the present experiments on Ar_nBr^- and Ar_nI^- combines the advantage of mass selectivity with much higher resolution (ca. 2–3 cm^{-1} for atomic systems) than PES experiments. This resolution allows accurate measurement of electron affinities, as well as spectroscopic observation of the electronic structure of the neutral Ar_nX clusters. The $Ar-X^-$ and $Ar-X$ pair potentials are known accurately from our previous work on the diatomic species.[4] Thus, by employing simulated annealing procedures to determine the binding energies and neutral electronic structure from model potentials, we can directly compare our experimental results with the pairwise additive predictions and explore the effects of various many-body corrections to the additive potentials. From this comparison, we can obtain a detailed picture of nonadditive effects in Ar_nX^- and Ar_nX clusters.

This article is organized as follows. In Sec. II we briefly describe the experimental apparatus and techniques. In Sec. III, we present the anion ZEKE and PDTP spectra, determine the experimental EAs, assign the electronic structure observed in the ZEKE spectra, and briefly discuss the observed vibrational structure. In Sec. IV, we describe the methods and present the results of calculations of the cluster EAs and

neutral electronic structure from model additive and nonadditive potential, and compare them with the experimental results. In Sec. V, we summarize, considering what we can and cannot conclude about many-body interactions on the basis of our results and suggest future avenues for experimental and theoretical research.

II. EXPERIMENT

Zero electron kinetic energy (ZEKE) spectroscopy was first developed for photoionization of neutrals by Müller-Dethlefs, Sander, and Schlag[19] and applied to negative ion photodetachment by Neumark and co-workers.[20] The experimental apparatus has been described in detail elsewhere.[20] Briefly, Ar_nX^- clusters are produced by expanding a mixture of approximately 0.1–0.5 % Freon (CF_3I or CF_2C1Br, PCR Co.) in a ca. 75% argon/25% helium mixture through a pulsed valve (General Valve Series 9) with a 0.5-mm-diam orifice. Backing pressures are typically 60–80 psi. The expansion is crossed with a 1 keV electron beam. Halide anions are formed by dissociative attachment of low energy secondary electrons and undergo clustering in the continuum flow region of the free expansion. The molecular beam is collimated with a skimmer, accelerated to 1 keV, and mass-selected with a 1 m long collinear time-of-flight mass spectrometer.[20(c),21] The mass-selected ions then enter a differentially pumped detection region and are irradiated with a pulse from an excimer pumped dye laser (Lambda Physik). For the ground states of Ar_nI BBQ, PBBO, Exalite 398, QUI, and DMQ laser dyes (Exciton) were used. For the $Ar_{2-3}I$ excited state scans rhodamine 610 dye was frequency doubled with a potassium dihydrogen phosphate (KDP) crystal. For the Ar_nBr clusters, DMQ and PTP dyes were used for the ground states; rhodamine 640 was doubled with a KDP crystal for the excited state $Ar_{2-3}Br$ spectra. The power of the undoubled light was typically 7–20 mJ per pulse at the interaction region. The frequency-doubled laser power was about 2 mJ per pulse. The laser wavelength was calibrated from 337 to 400 nm with the Ne lines observed by the optogalvanic effect in a Fe–Ne hollow cathode lamp. The fundamental wavelength of the frequency-doubled light was calibrated in the region 600–640 nm with an iodine absorption cell.

Two modes of electron detection were used in the present studies: the high resolution ZEKE mode, and the lower resolution partially discriminated threshold photodetachment (PDTP) mode. In the ZEKE mode, the photodetached electrons are extracted collinearly by a weak (2–5 V/cm) electric field after a 300–500 ns delay and deflected to an off-axis microchannel detector. Detection is gated to provide temporal filtering. A series of a apertures between the detachment point and detector provide spatial discrimination. This combination of spatial and temporal filtering discriminates against high energy electrons, so that as the laser wavelength is scanned, only photoelectrons with nearly zero kinetic energy are detected. The resolution of the instrument is about 2–3 cm^{-1} for atomic systems.[20] However, in the spectra of molecules, the peaks are broadened by unresolved rotational structure. For the systems studied in this article, the observed peaks were at least 8 cm^{-1} wide [full width at half maximum (FWHM)].

In the PDTP mode,[20(b)] there is no delay between the laser pulse and electron extraction, retaining only spatial filtering as in the ''steradiancy detector'' first described by Baer, Peatman, and Schlag[22] and Spohr *et al.*[22] This results in some discrimination against electrons with energies greater than about 150 cm^{-1} and leads to peaks about 200 cm^{-1} wide in the present case. However, the thresholds, and hence the electron affinities, can be determined more accurately than this, to within approximately ± 50 cm^{-1}. Because nearly all of the electrons are collected, this mode of operation has the advantage of much higher sensitivity than the ZEKE mode.

The ZEKE spectra were averaged over several thousand laser shots per point taken in several separate scans. The PDTP spectra were averaged over 300–1000 laser shots per point. All spectra were normalized to the ion signal and laser power.

No obvious ''magic numbers'' were seen in the mass spectra. The ion signal smoothly decreased in intensity with increasing cluster size in the mass spectra of both the Ar_nBr^- and Ar_nI^- clusters.

III. RESULTS

A. $Ar_{2-3}I^-$ and $Ar_{2-3}Br^-$

The ZEKE spectra of Ar_2Br^- and Ar_3Br^- are shown in Fig. 1, along with the spectrum of the diatomic $ArBr^-$ complex, reproduced from Ref. 4. ZEKE spectra of ArI^-, Ar_2I^-, and Ar_3I^- are displayed in Fig. 2. All the spectra have two sets of features, separated by approximately the spin–orbit splitting of the halogen atoms: 3685 cm^{-1} for Br and 7603.15 cm^{-1} for I.[23] We assign the lower energy set of features to electronic states arising from the ground $^2P_{3/2}$ state of the halogen atom and the higher energy features to $^2P_{1/2}$ asymptotic states. The ground state manifolds of the $Ar_{2-3}I$ clusters are dominated by two sharp, intense peaks, labeled X and I, separated by about 40–65 cm^{-1}. In the $Ar_{2-3}Br$ spectra, both features are also present, but peak I is less intense and distinct than in the Ar_nI spectra.

In the previous work on the diatomic species[4] the corresponding features were assigned to the origins of the two electronic states that correlate to the halogen $^2P_{3/2}$ asymptote, referred to as the $X\frac{1}{2}$ ($j_a=\frac{1}{2}$, $\Omega=\frac{1}{2}$) and $I\frac{3}{2}$ ($j_a=\frac{3}{2}$, $\Omega=\frac{3}{2}$) states, in Hund's case (c) notation.[24] The feature labeled $II\frac{1}{2}$ in the diatomic spectra was assigned to the origin of the $II\frac{1}{2}$ state ($j_a=\frac{3}{2}$, $\Omega=\frac{1}{2}$), which correlates to the halogen $^2P_{1/2}$ asymptote. We expect an analogous set of three doubly degenerate electronic states to be present in the polyatomic clusters. The lower $^2P_{3/2}$ halogen state is split into two doubly degenerate states by the weak interaction with the argon atoms. We refer to these states as the X and I states, by analogy with the diatomic case, dropping the Ω designation, as this is no longer a good quantum number in the polyatomic case. Note that here the ''X state'' always refers to

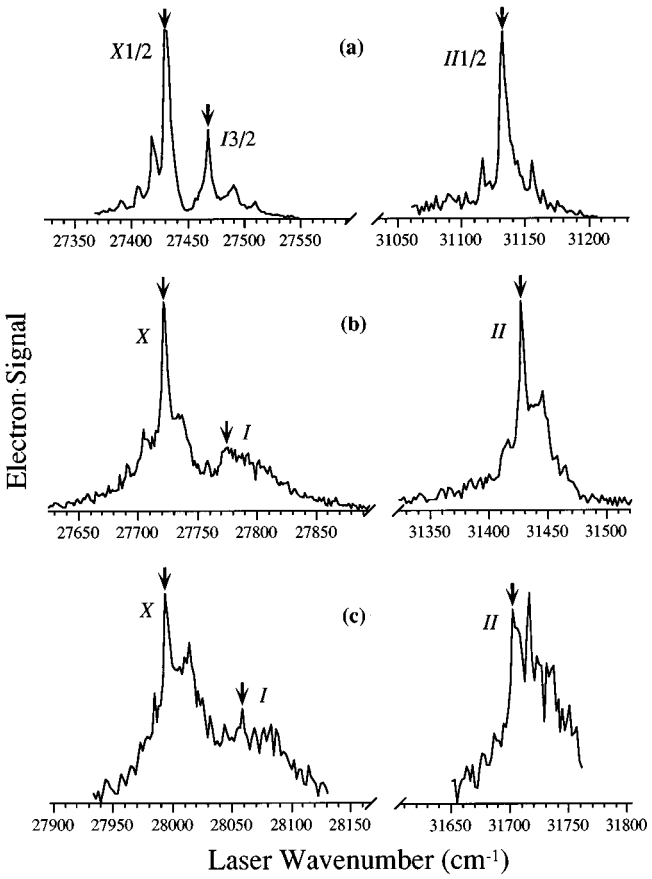

FIG. 1. ZEKE spectra of (a) $ArBr^-$, (b) Ar_2Br^-, and (c) Ar_3Br^-. The arrows indicate the neutral electronic state origins.

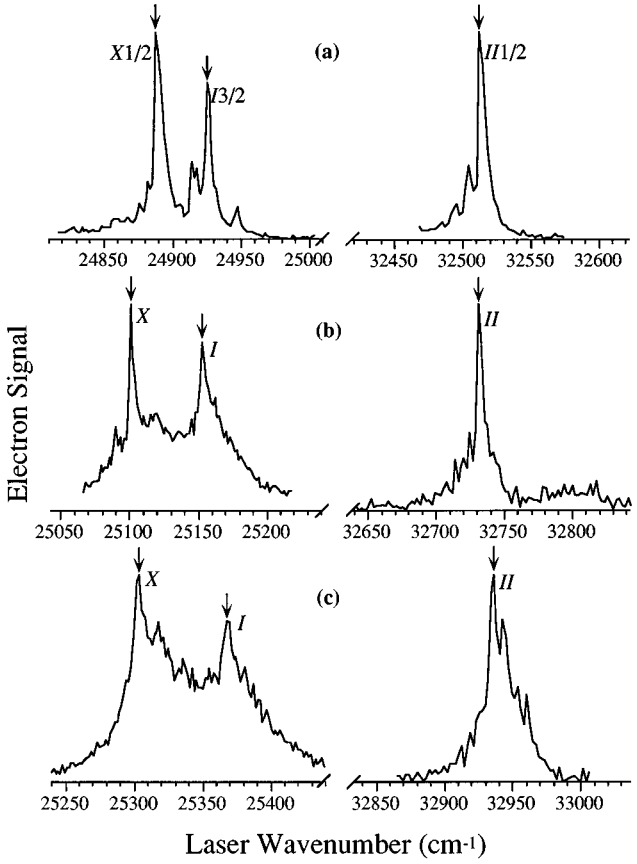

FIG. 2. ZEKE spectra of (a) ArI^-, (b) Ar_2I^-, and (c) Ar_3I^-. The arrows indicate the neutral electronic state origins.

the lowest energy state at the equilibrium geometry regardless of the symmetry of the cluster.

The *X* and *II* state origins are blue shifted relative to the corresponding atomic lines by several hundred cm^{-1}. The blue shift increases as the number of argon atoms increases. This demonstrates that the anionic clusters are more strongly bound than the neutral species.

In the Ar_2Br^- spectrum [Fig. 1(b)] we see some partially resolved peaks to the red and blue of the *X* state origin. There is also a long ''tail'' to the blue of the *I* state origin. We attribute all these features to transitions to or from vibrationally excited states. Based on our previous interpretation of the diatomic $ArBr^-$ spectrum,[4] it is likely that the features to the red of the *X* state origin are due to hot-band or sequence-band transitions from vibrationally excited anion states. Likewise, the features to the blue of the *X* state origin may be transitions to vibrationally excited neutral ground states and/or hot-band transitions to the *I* state. The vibrational progressions are not as well resolved as in the diatomic spectra. The observed structure is probably due to many overlapping transitions involving more than one vibrational mode. This spectral congestion appears to be more severe to the blue of the *I* state origin, possibly indicating a larger geometry change between the *I* state and the anion than between the *X* state and the anion, as was seen in $ArBr^-$.[4] The peaks to the red and blue of the II state origin may similarly be understood as sequence-band or hot-band transitions, and transitions to vibrationally excited neutral states, respectively.

The spectrum of Ar_3Br^- [Fig. 1(c)] appears even more congested. There is a distinct peak 20 cm^{-1} to the blue of the *X* state origin, in addition to numerous poorly resolved features. Again there appears to be an extended unresolved progression to the blue of the *I* state-origin. The *II* state has two prominent peaks, separated by 14 cm^{-1}, plus some other indistinct peaks to the blue. It is not clear which of the two peaks is in fact the *II* state origin.

In the case of Ar_2I^- [Fig. 2(b)], the vibrational structure is somewhat less well resolved than that in Ar_2Br^-. There is a clear feature 11 cm^{-1} to the red of the *X* state origin, as well as some poorly resolved structure between the origins of the *X* and *I* states. There is a tail to the blue of the *I* state origin. The spectrum of the *II* state is rather sparse, with some peaks 10–30 cm^{-1} to the red of the origin due to sequence or hot bands, and a slight shoulder to the blue. The lack of any extended progression indicates that the anion–*II* state transition is quite vertical.

The spectrum of Ar_3I^- [Fig. 2(c)] shows clearer vibrational resolution than Ar_2I^-. There are two peaks spaced by 8 and 32 cm^{-1} to the blue of the *X* state origin. However, the

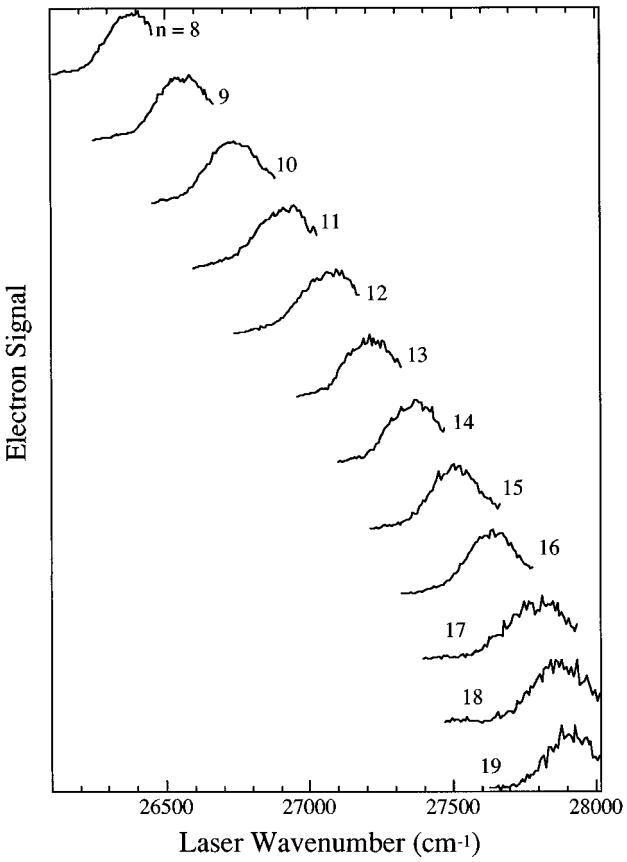

FIG. 5. PDTP spectra of $Ar_{8-19}I^-$.

sequence-band structure to the red of the origin is not resolved. The *II* state of Ar_3I displays three distinct peaks, 7, 17, and 24 cm^{-1} to the blue of the origin, as well as some less distinct sequence-band structure to the red.

The partially resolved vibrational structure seen in these spectra is of considerable interest and will be considered further in future publications. In this article, we are primarily concerned with the accurate electron affinities and state splittings yielded by these spectra.

B. $Ar_{4-7}I^-$

The ZEKE spectra of the $Ar_{4-7}I^-$ clusters are shown in Fig. 3. For these clusters we studied only the lower ($^2P_{3/2}$ asymptotic) states. In the Ar_4I spectrum [Fig. 3(a)] the origins of the *X* and *I* electronic states are distinct. In the Ar_5I spectrum [Fig. 3(b)] the peak corresponding to the *X* state origin is quite broad, and the *I* state appears as an unresolved shoulder. The *I* state also appears relatively less intense than in the $Ar_{1-4}I$ spectra. Based on the profile of this shoulder, we can only estimate the position of the *I* state origin to ± 20 cm^{-1}.

The spectra of Ar_6I and Ar_7I [Fig. 3(c) and 3(d)] are more congested. The positions of the *X* and *I* state origins can be estimated, as indicated by the arrows in the figures, but it is not possible to discern any reproducible vibrational structure. As we go from Ar_4I to Ar_7I, the separation between the *X* and *I* states appears to decrease. Although the exact splitting is difficult to discern from the Ar_6I^- spectrum, it appears in this case that the $X-I$ splitting again decreases somewhat from Ar_5I. However, the splitting appears to increase again in the Ar_7I spectrum, in which the two states are better resolved than in the Ar_6I spectrum.

We attempted to observe ZEKE spectra of Ar_8I^- and larger clusters, but obtained only unstructured spectra with no reproducible features.

C. Partially discriminated threshold photodetachment spectra

Because of the increasing spectral congestion with increasing cluster size and the difficulty of producing sufficient quantities of large clusters with our source, it was not possible to perform the ZEKE experiment on clusters with $n>7$ in the case of Ar_nI^-, and $n>3$ for Ar_nBr^-. In the PDTP mode of operation it is possible to work with much smaller quantities of anions, because nearly all of the photoelectrons near the detachment threshold are collected. Therefore, only the PDTP experiment was performed for $Ar_{4-9}Br^-$ and $Ar_{8-19}I^-$.

The PDTP spectra of $Ar_{4-9}Br^-$ are described below. We demonstrate that the experimentally observed cluster properties are not consistent with pairwise addition potentials, and then we add three-body nonadditive corrections to the potentials.

TABLE I. Experimental adiabatic electron affinities, excited state origins, and electronic state splittings for Ar_nBr. All energies are in cm^{-1}. Uncertainties given are in parentheses.

n	EA (X state origin)	I state origin	Δ_{X-II}
0	27 129.2[a]	30 814[a]	3685[b]
1	27 489.6 (3.0)	27 467.1 (1.6)	
2	27 723.4 (3.0)	27 775.5 (5.0)	
3	27 994.6 (3.0)	28 059.4 (1.6)	
4	28 266 {50}	…	
5	28 532 {50}	…	
6	28 778 {50}	…	
7	29 021 {50}	…	
8	29 259 {50}	…	
9	29 491 {50}	…	

…	…	…
37.8 (2.3)	31 132.3 (1.6)	3702.7 (3.4)
53.1 (5.5)	31 427.8 (2.2)	3705.4 (3.7)
64.8 (2.3)	31 702.8 (2.2)	3708.2 (3.7)
…	…	…
…	…	…
…	…	…
…	…	…
…	…	…
…	…	…

[a]C. Blondel, P. Cacciani, C. Delsart and R. Trainham, Phys. Rev. A **40**, 3698 (1989).
[b]C. E. Moore, *Atomic Energy Levels*, Natl. Bur. Std. 467 (1949), Vol. 1.

TABLE II. Experimental adiabatic electron affinities, excited state origins, and electronic state splittings for Ar_nI. All energies are in cm^{-1}. Uncertainties are given in parentheses.

n	EA (X state origin)	I state origin	Δ_{X-I}	II state origin	Δ_{X-II}
0	24673.3[a]	⋯	⋯	32 276.5[a,b]	7603.15[b]
1	24 888.3 (3.0)	24 925.5 (1.5)	37.2 (2.2)	32 512.6 (2.2)	7624.3 (3.7)
2	25 100.9 (3.0)	25 152.9 (3.0)	52.0 (3.4)	32 731.2 (2.2)	7630.3 (3.7)
3	25 303.0 (3.0)	25 368.0 (4.5)	65.0 (5.1)	32 936.4 (2.2)	7633.4 (3.7)
4	25 502.2 (3.0)	25 571 (10)	69 (10)	⋯	⋯
5	25 702 (10)	25 762 (10)	60 (14)	⋯	⋯
6	25 907 (15)	25 950 (15)	43 (21)	⋯	⋯
7	26 083 (15)	26 163 (10)	60 (18)	⋯	⋯
8	26 247 (50)	⋯	⋯	⋯	⋯
9	26 413 (50)	⋯	⋯	⋯	⋯
10	26 582 (50)	⋯	⋯	⋯	⋯
11	26 753 (50)	⋯	⋯	⋯	⋯
12	26 904 (50)	⋯	⋯	⋯	⋯
13	27 079 (50)	⋯	⋯	⋯	⋯
14	27 226 (50)	⋯	⋯	⋯	⋯
15	27 375 (50)	⋯	⋯	⋯	⋯
16	27 488 (50)	⋯	⋯	⋯	⋯
17	27 617 (50)	⋯	⋯	⋯	⋯
18	27 717 (50)	⋯	⋯	⋯	⋯
19	27 794 (50)	⋯	⋯	⋯	⋯

[a]H. Hotop and W. C. Lineberger, J. Phys. Chem. Ref. Data **14**, 731 (1985).
[b]C. E. Moore, *Atomic Energy Levels*, Circ. Natl. Bur. Std. 467 (1949), Vol. 1.

A. Pair potentials

The pair potential of the ArBr neutral has been determined in scattering experiments by Lee and co-workers.[27] The scattering experiments characterized only the neutral $X\frac{1}{2}$ and $I\frac{3}{2}$ state potentials. Our previous ZEKE results[4] on the ArBr complex provided further refinement of the potential of Ref. 27, as well as information on the neutral $II\frac{1}{2}$ state and anion potentials. In the case of ArI, scattering results are not available, so the ZEKE spectrum is the only source of information on the ArI diatomic potentials.

The neutral Ar–X potentials are of the Morse–Morse-switching function–van der Waals (MMSV) form. The reduced form of this potential, with $x=r/r_m$ and $f(x)=V(r)/\epsilon$, is

$$\begin{aligned} f(x) &= e^{2\beta_1(1-x)}-2e^{\beta_1(1-x)}, \quad 0<x\leqslant 1 \\ &= e^{2\beta_2(1-x)}-2e^{\beta_2(1-x)}\equiv M_2(x), \quad 1<x\leqslant x_1 \\ &= \mathrm{SW}(x)M_2(x)+[1-\mathrm{SW}(x)]W(x), \quad x_1<x<x_2 \\ &= -C_{6r}x^{-6}-C_{8r}x^{-8}\equiv W(x), \quad x_2\leqslant x<\infty, \end{aligned} \tag{6}$$

where ϵ is the well depth, r_m is the bond length, and the switching function is given by

$$\mathrm{SW}(x)=\frac{1}{2}\left(\cos\frac{\pi(x-x_1)}{x_2-x_1}+1\right). \tag{7}$$

The reduced dimensionless coefficients C_{6r} and C_{8r} are related to the usual dispersion coefficients C_6 and C_8 by

$$C_{6r}=\frac{C_6}{\epsilon r_m^6}, \quad C_{8r}=\frac{C_8}{\epsilon r_m^8}. \tag{8}$$

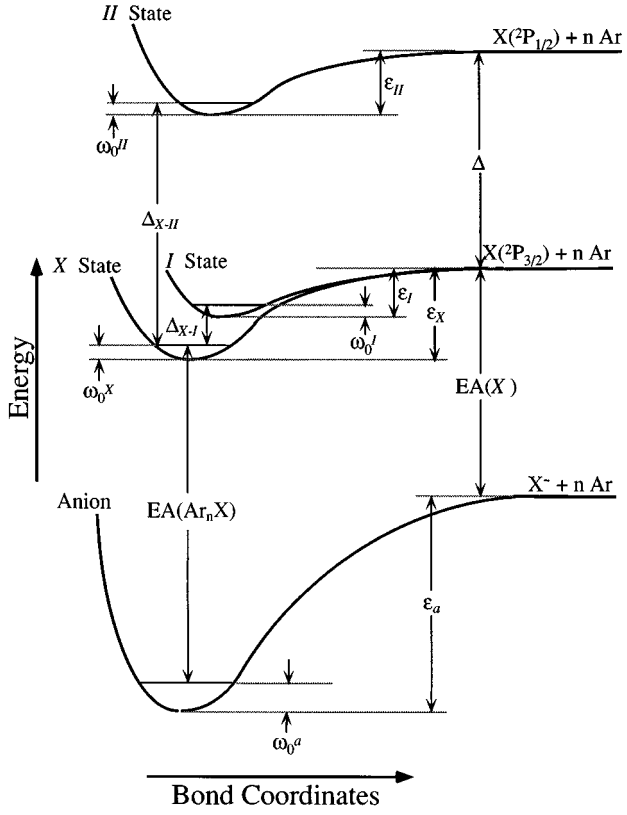

FIG. 6. Schematic energy level diagram of the Ar_nX^- anion and Ar_nX neutral electronic states.

TABLE III. MMSV pair potential parameters of argon halides.

	ArI				ArBr			
	$X\,^2\!\!\frac{1}{2}$	$I\,^2\!\!\frac{1}{2}$	$II\,^2\!\!\frac{1}{2}$	Anion	$X\,^2\!\!\frac{1}{2}$	$I\,^2\!\!\frac{3}{2}$	$II\,^2\!\!\frac{1}{2}$	Anion
ϵ (meV)	18.8	13.9	16.0	45.8	16.5	11.5	14.0	54.4
r_m (Å)	3.95	4.18	4.11	4.07	3.73	3.94	3.89	3.78
β_1	7.15	7.25	6.90	5.70	6.80	7.72	6.70	5.10
β_2	6.18	6.30	6.40	4.45	6.50	7.10	6.35	4.45
x_1	1.01	1.04	1.04	1.08	1.02	1.012	1.01	1.065
x_2	1.62	1.62	1.64	1.62	1.59	1.63	1.58	1.66
C_6 (eV Å^6)	98.4	98.4	98.4	⋯	65.2	70.2	68.8	⋯
C_8 (eV Å^8)	715	715	715	⋯	379	379	379	⋯
B_4 (eV Å^4)	⋯	⋯	⋯	12.8	⋯	⋯	⋯	12.5
B_6 (eV Å^6)	⋯	⋯	⋯	162	⋯	⋯	⋯	120.5

The anion potentials have the same form, except that the van der Waals portion is replaced by a function including charge-induced dipole (r^{-4}) and charge-induced quadrupole and dispersion (r^{-6}) terms:

$$f(x) = -B_{4r}x^{-4} - B_{6r}x^{-6} \equiv W(x), \quad x_2 \leqslant x < \infty \tag{9}$$

with

$$B_{4r} = \frac{B_4}{\epsilon r_m^4}, \quad B_{6r} = \frac{B_6}{\epsilon r_m^6}. \tag{10}$$

Further details about the construction of the Ar–Br and Ar–I pair potentials are given in Ref. 4.

The MMSV potential parameters used in this work are given in Table III. Some of the parameters used here have been modified slightly from those published previously.[4] The reason for this is that in the previous work, the well depths of the three neutral electronic states and the anion were related to each other using the relationships implied by Fig. 6, with the zero point energies used in these relations assumed to be equal to half of the observed vibrational fundamental frequencies. A slightly more accurate procedure, used to obtain the parameters in Table III, is to calculate the actual zero point energies from the model potentials. The well depth parameters are then iteratively adjusted in order to satisfy Eqs. (3)–(5), as well as to fit the observed spectra. The well depths obtained in this way differ from those given previously by no more than 2–3 cm^{-1}, which is within the uncertainties stated in Ref. 4.

It is important here to consider the uncertainties in the pair potential parameters. In the case of the ArBr potentials, the scattering experiments provide information on the absolute values of the well depths and bond lengths for the $X\,^2\!\!\frac{1}{2}$ state. On the other hand, the ZEKE spectra, although quite sensitive to the *relative* bond lengths and well depths between the anion and neutral states, are not very sensitive to the *absolute* values of these parameters. Therefore, the r_m and ϵ parameters for the $X\,^2\!\!\frac{1}{2}$ state of ArBr were fixed at the values of Lee and co-workers.[27] The parameters for the anion and remaining neutral states were then adjusted to be consistent with the relations implied by Fig. 6, as well as to reproduce the ZEKE spectrum. The uncertainties in r_m and ϵ stated in Ref. 27 are ±0.2 Å and ±9 cm^{-1}, respectively, so the absolute uncertainties of r_m and ϵ for the anion and the other neutral states are of about the same order. However, the *relative* uncertainties in r_m and ϵ between the anion and neutral are significantly smaller than this. For example, because the uncertainty in the EA obtained from the ZEKE spectrum is ±3 cm^{-1}, the difference $\epsilon_a - \epsilon_X$ is known with about this same uncertainty. [See Eq. (2)]. Similarly, the relative uncertainties in r_m are found to be about 1–2 % (0.04–0.08 Å), based on the fit to the ZEKE spectra.

For ArI, for which scattering experiments have not been performed, modified versions of the polarizability correlation formulas of Pirani and co-workers[28] were used to estimate r_m and ϵ for the $II\,^2\!\!\frac{1}{2}$ state of ArI, as described in Ref. 4. Then the remaining neutral and anion potentials were adjusted to fit the ZEKE spectrum. The estimated *absolute* uncertainties in r_m and ϵ of ArI are ±18 cm^{-1} for ϵ and ±0.2 Å for r_m. However, the same considerations about the *relative* uncertainties among the anion and neutral states also apply for ArI. The relative uncertainties in ϵ and r_m are ±3 cm^{-1} and ±0.04–0.08 Å, respectively.

To model the Ar–Ar pair interaction, the accurate Hartree–Fock dispersion (HFD-B2) potential of Aziz and Slaman[29] was used. For this potential r_m=3.7565 Å and ϵ=99.5465 cm^{-1}. For the detailed form and other parameters of this well-known potential, see Ref. 29.

The pairwise additive approximations to the Ar_nBr^- and Ar_nI^- binding energies were found by minimizing the additive potentials, using the simulated annealing procedure to be described below, from

$$\epsilon_a = \min(V_{\mathrm{ArX}} + V_{\mathrm{ArAr}}), \tag{11}$$

with $V_{\mathrm{ArX}} = \Sigma_i V_{i0}(|\mathbf{r}_i - \mathbf{r}_0|)$, and $V_{\mathrm{ArAr}} = \Sigma_{i<j} V_{ij}(|\mathbf{r}_i - \mathbf{r}_j|)$, where the sums run over the Ar atoms, $\mathbf{r}_i$ is an Ar atom position, and $\mathbf{r}_0$ is the halide position. The calculation of the neutral potentials is more complex because of the open-shell nature of the halogen atom and is discussed in Sec. IV E.

B. Simulated annealing method

We use a simple molecular dynamics simulated annealing procedure to determine the minimum energy cluster geometries. The simulated annealing program used here was

adapted from a molecular dynamics program written by Li and co-workers.[30] The procedure used is as follows:

(1) Random initial atomic positions are generated. The initial positions lie within a 6–15 Å box, depending on the size of the cluster, and are subject to the constraint that no two atoms may be closer than a certain cutoff distance, usually 3.5 Å. The latter condition ensures that the cluster starts out in an attractive region of the potential surface so that dissociation does not occur.

(2) The classical equations of motion are solved for about 5 ps, using a Gear predictor–corrector algorithm started with a 16 step Runge–Kutta algorithm.[30] The step size is 5 fs.

(3) Kinetic energy is removed by rescaling the atomic velocities. When starting with random positions, the kinetic energy is removed very quickly, so that the velocities and kinetic energies are essentially reset to zero with each rescaling. This rapid quenching was found to be necessary to prevent evaporation.

(4) Steps (2) and (3) are repeated until a minimum is found. This typically requires 100–250 ps.

(5) Beginning with the minimum configuration found by the above procedure, kinetic energy is added, constrained so that the translational energy of the cluster center of mass and its angular momentum are zero. To prevent evaporation, the initial kinetic energy was usually set to not more than 25–33 % of the total well depth. Then steps (2) and (3) are repeated, but with kinetic energy removed much more gradually, by rescaling the velocities by a factor[31]

$$\left[1+\frac{\tau_{\text{scale}}}{\tau_{\text{const}}}\left(\frac{\text{KE}_{\text{targ}}}{\text{KE}_{\text{av}}}-1\right)\right]^{1/2}$$

every 5 ps. Here τ_{scale} is the time between rescalings, τ_{const} is a time constant (typically 50 or 100 ps), KE_{av} is the average kinetic energy, and KE_{targ} is a target kinetic energy, set to a very small value in order to find a minimum. The entire procedure typically requires 5–10 ns.

(5)Finally, the minimum energy configuration is located more precisely using a simple gradient minimization routine.[32]

The entire annealing procedure was repeated 5–20 times for each cluster to ensure that the global minimum was found. In this process, low-lying local minima were often also found. In order to locate higher-lying local minima, an interval of 250 fs or less between rescaling steps is used in steps (2)–(4), to prevent equilibration of the cluster as kinetic energy is removed.

C. Zero point energy calculation

Once the minimum energy configurations and classical binding energies are found, it is necessary to know the zero point energies in order to use Eqs. (3)–(5). The model potentials are analytical functions of the nuclear Cartesian coordinates, allowing the zero point energies to be estimated by the following procedure. The normal coordinates of the clusters were found in terms of linear combinations of Cartesian displacement coordinates, using standard techniques.[33] Then each of the $3N-6$ single-mode vibrational Schrödinger equations was solved using a simple one-dimensional discrete variable representation (DVR) procedure.[5,34–36] The total zero point energy was then obtained by adding up the single-mode values. In this way, the anharmonicity of the potential is approximately accounted for, although interactions between normal modes are neglected. The zero point energy calculation was limited to the portion of the potential in the vicinity of the minimum structure, so that any splittings due to tunneling are not reproduced.

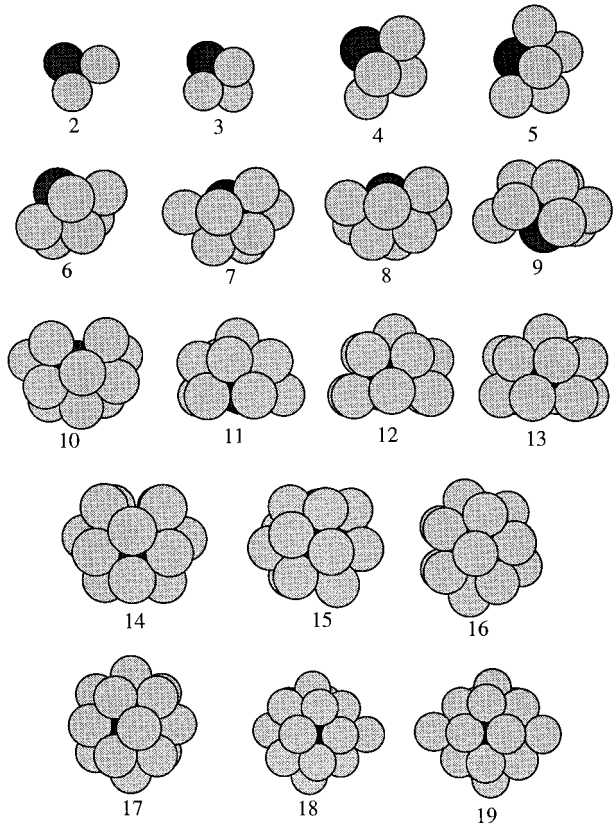

FIG. 7. Minimum energy structures of $Ar_{2-19}I^-$ clusters found using pairwise additive potentials.

D. Anion minimum energy geometries

The minimum energy geometries found using pairwise additive potentials for $Ar_{2-19}I^-$ are shown in Fig. 7. Similar structures were found for $Ar_{2-9}Br^-$. The calculated anion binding energies and zero point energies are given in Tables IV and V.

For $Ar_{2-3}X^-$ (X=Br or I), there is only one minimum, in which all atoms are in contact with each other. Linear (Ar_2X^-) or planar (Ar_3X^-) geometries are not stable with additive potentials.

In the minimum energy structures of larger clusters (Ar_nI^-, $4\leqslant n\leqslant 17$, and Ar_nBr^-, $4\leqslant n\leqslant 9$), all the Ar atoms contact the central halide atom. This type of structure is energetically favorable because each Ar–X^- ''bond'' is about four times stronger than an Ar–Ar ''bond.'' For Ar_4X^-, one

TABLE IV. Results of calculations with pairwise additive Ar^nBr^- anion potentials, and ''matrix-additive'' Ar_nBr neutral potentials. All energies are in cm^{-1}.

n	ϵ_a	ω_0^a	ϵ_x	ω_0^X	ϵ_I	ω_0^I	Δ_{X-I}	ϵ_{II}	ω_0^{II}	Δ_{X-II}	EA_{add}
0	0	0	0	0	0	0	0	0	0	3685[a]	27129.2[b]
1	438.8	20.7	133.1	15.6	92.8	13.5	38.2	112.9	13.4	3703.0	27429.8
2	977.1	56.8	349.4	42.3	295.4	45.0	56.6	319.6	44.6	3717.1	27742.3
3	1614.9	107.4	662.6	85.1	599.9	89.6	67.3	628.7	88.6	3722.4	28059.2
4	2260.0	157.8	977.3	127.6	916.6	135.2	68.4	945.0	132.9	3722.6	28382
5	2911.3	207.5	1293.6	168.7	1243.7	181.1	62.3	1267.3	176.4	3719.0	28708
6	3659.7	267.5	1696.2	211.7	1677.2	248.5	55.8	1686.0	230.0	3713.6	29037
7	4318.6	315.5	2042.9	268.9	2001.2	289.7	62.5	2014.8	272.9	3717.1	29358
8	5069.8	371.1	2465.0	315.8	2413.9	337.1	72.4	2432.4	323.6	3725.4	29679
9	5815.2	421.3	2880.0	360.3	2807.1	375.7	88.2	2837.7	370.1	3737.1	30003

[a]C. E. Moore, *Atomic Energy Levels*, Circ. Natl. Bur. Std. 467 (1949), Vol. 1.
[b]C. Blondel, P. Cacciani, C. Delsart, and R. Trainham, Phys. Rev. A **40**, 3698 (1989).

local minimum isomer is seen (C_{3v} point group) which has one Ar atom in contact with the other three argons but not with the halide. In Ar_4I^-, its energy is about 200 cm^{-1} higher than that of the global minimum. The analogous Ar_4Br^- isomer lies 256 cm^{-1} above the global minimum. These energy differences correspond approximately to one $Ar–X^-$ ''bond.'' Ar_5X^- has two local minima with approximately the same separations from the global minimum as in the Ar_4X^- clusters.

The clusters with $6 \leqslant n \leqslant 17$ show two types of local minima. In one type, the Ar atoms are all in contact with the halide—as in the global minimum—but have fewer Ar–Ar ''bonds.'' These typically differ in energy from the global minimum by approximately the magnitude of an Ar–Ar ''bond,'' i.e., about 100 cm^{-1}. The other type, seen already for $n<6$, are structures in which one or more Ar atoms are not in direct contact with the halide. This type of isomer usually differs in energy from the global minimum by approximately the energy of one or more $Ar–X^-$ ''bonds.''

For Ar_nI^-, rare gas atoms continue to fit around the halide without significant crowding up to $n=15$. At $n=16$ there is some crowding, so that the $Ar–I^-$ contribution to the potential is reduced. $Ar_{17}I^-$ constitutes a ''closed'' solvent shell (at 0 K). It consists of a capped pentagonal bipyramid structure (D_{5h}), with the axial Ar atoms significantly further from the halide than the others. Subsequent Ar atoms are added outside the first solvent shell. In the case of Ar_nBr^-, we did not observe the closing of the solvent shell since we did not perform calculations for $n>9$.

E. Neutral open-shell potentials

Because of the anisotropy of the open-shell halogen atom in the neutral clusters, the potentials cannot in general

TABLE V. Results of calculations with pairwise additive Ar_nI^- anion potentials, and ''matrix-additive'' Ar_nI neutral potentials. All energies are in cm^{-1}.

n	ϵ_a	ω_0^a	ϵ_X	ω_0^X	ϵ_I	ω_0^I	Δ_{X-I}	ϵ_{II}	ω_0^{II}	Δ_{X-II}	EA_{add}
0	0	0	0	0	0	0	0	0	0	7603.15[a]	24673.3[b]
1	369.4	17.3	151.6	14.6	112.1	12.3	37.2	129.0	13.2	7624.4	24888.3
2	838.4	51.0	385.4	41.2	332.0	42.4	54.5	355.5	42.4	7634.3	25116.5
3	1406.8	98.4	718.1	83.2	653.1	85.8	67.6	682.5	85.4	7640.9	25346.8
4	1982.0	145.8	1051.5	125.1	986.0	130.1	70.5	1016.3	128.7	7642.0	25583
5	2562.3	192.7	1385.6	165.8	1328.5	174.9	66.2	1355.1	171.3	7639.2	25823
6	3229.2	249.4	1799.2	208.3	1767.6	233.9	57.3	1782.7	222.5	7633.8	26062
7	3815.2	295.3	2151.3	257.8	2112.5	279.6	60.6	2126.9	264.3	7634.0	26300
8	4469.2	343.5	2569.3	300.4	⋯	⋯	⋯	⋯	⋯	⋯	26530
9	5094.8	379.9	2963.2	334.7	⋯	⋯	⋯	⋯	⋯	⋯	26760
10	5731.8	436.9	3369.0	390.0	⋯	⋯	⋯	⋯	⋯	⋯	26990
11	6366.8	476.1	3764.8	428.1	⋯	⋯	⋯	⋯	⋯	⋯	27227
12	7044.3	539.6	4199.3	483.9	⋯	⋯	⋯	⋯	⋯	⋯	27463
13	7796.7	586.8	4706.4	530.4	⋯	⋯	⋯	⋯	⋯	⋯	27707
14	8519.3	645.1	5159.0	572.8	⋯	⋯	⋯	⋯	⋯	⋯	27961
15	9280.6	710.5	5686.6	641.6	⋯	⋯	⋯	⋯	⋯	⋯	28198
16	9914.3	777.5	6143.3	693.7	⋯	⋯	⋯	⋯	⋯	⋯	28360
17	10561.3	850.4	6589.0	770.0	⋯	⋯	⋯	⋯	⋯	⋯	28565
18	11102.2	913.0	7061.3	804.9	⋯	⋯	⋯	⋯	⋯	⋯	28606
19	11648.0	979.3	7498.0	880.8	⋯	⋯	⋯	⋯	⋯	⋯	28725

[a]C. E. Moore, *Atomic Energy Levels*, Circ. Natl. Bur. Std. 467 (1949), Vol. 1.
[b]H. Hotop and W. C. Lineberger, J. Phys. Chem. Ref. Data **14**, 731 (1985).

be obtained by simply adding the Ar–X pair potentials. This is clear from the observed spectra. For example, in the diatomic ArI molecule an $X-I$ splitting of 37 cm^{-1} is observed.[4] If the potentials were simply additive, one would predict an $X-I$ splitting of 74 cm^{-1} for Ar_2I. The observed Δ_{X-I} in Ar_2I is 52 cm^{-1}. The simple additive prediction is well outside experimental uncertainty.

This ''nonadditivity'' of the open-shell potentials has been discussed by Lawrence and Apkarian,[37] whose explanation we follow here. The nonadditivity can most easily be understood if we momentarily neglect the effect of spin–orbit coupling. In this case there are two electronic states of the diatomic complex corresponding to the two possible orientations of the singly occupied halogen p orbital relative to the argon atom.[24,38] A $^2\Sigma$ state arises when the singly occupied p orbital lies along the internuclear axis, and a doubly degenerate $^2\Pi$ state corresponds to the singly occupied p orbital lying perpendicular to the internuclear axis. However, if the cluster contains additional Ar atoms, Λ is no longer a good quantum number if the polyatomic cluster is not linear. Consider, for example, the case of Ar_2I. The singly occupied halogen p orbital will not, in general, lie either parallel or perpendicular to either of the Ar–I internuclear axes. Therefore the Ar–I interaction potentials in Ar_2I will not be the same as the potentials of either the $^2\Sigma$ or $^2\Pi$ diatomic states, but—in the first approximation—may be considered to be linear combinations of the diatomic potentials. Thus, in order to obtain the potentials of Ar_2I and larger open-shell clusters from the diatomic potentials, our concept of pairwise additivity must be *extended* to include this mixing of the diatomic electronic states. We describe how this is done in more detail below.

A simple first-order perturbation theory treatment of the interaction of an open-shell atom with several closed-shell (rare gas) atoms in terms of the diatomic potentials has been developed by various workers.[39–42] These methods have been used to study open-shell atoms in rare gas matrices, clusters, and on surfaces.[12,37,43–45] Our implementation here most closely resembles that of Lawrence and Apkarian,[37] who studied the emission spectra of I atoms in Xe and Kr matrices. The theory is briefly as follows.

The Ar_n–X interaction is modeled by an effective potential depending on the rare gas coordinates and on the coordinates of the ''hole'' in the singly occupied halogen p orbital in an arbitrary space-fixed frame:

$$H' = \sum_k V_{\mathrm{Ar}_n\mathrm{X}}(\mathbf{r},\mathbf{R}_k) + H_{\mathrm{SO}}. \tag{12}$$

Here, the sum is over the rare gas atoms, $\mathbf{r}$ is the coordinate of the ''hole,'' $\mathbf{R}_k$ are the rare gas coordinates relative to the halogen nucleus, and H_{SO} is the spin–orbit interaction Hamiltonian.

The potential $V_{\mathrm{Ar}_n\mathrm{X}}$ is then expanded in Legendre polynomials in $\hat{\mathbf{r}}\cdot\hat{\mathbf{R}}_k$. We are ultimately interested in the matrix elements of H' in a p-orbital basis, and only the first two even terms of the expansion contribute to these. Hence, we write

$$H' = \sum_k \left[V_0(r,R_k) + V_2(r,R_k)P_2(\hat{\mathbf{r}}\cdot\hat{\mathbf{R}}_k)\right] + H_{\mathrm{SO}}. \tag{13}$$

In the diatomic case (one Ar atom), the expectation values of these two expansion coefficients, $V_0(R)$ and $V_2(R)$, can be shown, using the relations given by Haberland[24] and Aquilanti *et al.*,[38] to be related to the spectroscopic diatom potentials by

$$V_0(R) = \tfrac{1}{3}\left[V_{X\frac{1}{2}}(R) + V_{I\frac{3}{2}}(R) + V_{II\frac{1}{2}}(R)\right]. \tag{14}$$

and

$$V_2(R) = \tfrac{5}{3}\left[V_{X\frac{1}{2}}(R) + V_{II\frac{1}{2}}(R) - 2V_{I\frac{3}{2}}(R)\right]. \tag{15}$$

Here, the zero for each potential is set at the potential asymptote. ($^2P_{1/2}$ for $V_{I\frac{3}{2}}$, and $^2P_{3/2}$ for $V_{X\frac{1}{2}}$ and $V_{II\frac{1}{2}}$). In deriving these equations it is assumed that the spin–orbit constant Δ is independent of R.

With some effort, one can show that for a cluster with many Ar atoms, the perturbation Hamiltonian $\mathbf{H}'$ is given by a 6×6 matrix:[37,42]

$$\mathbf{H}' = \sum_k V_0(R_k)\cdot\mathbf{1} + V_2(R_k)\cdot\mathbf{M}(\mathbf{R}_k), \tag{16}$$

where $\mathbf{M}(\mathbf{R}_k)$ is a 6×6 Hermitian matrix involving the argon atom coordinates. The detailed form of the matrix $\mathbf{H}'$ has been given, in the $|J,m_J\rangle$ basis, by Lawrence and Apkarian.[37] Diagonalization of $\mathbf{H}'$ yields three doubly degenerate eigenvalues, corresponding to the potentials of the X, I, and II states.

In our implementation, an analytical form for the eigenvalues was found using the Maple V program. This allowed the eigenvalues to be calculated approximately 10 times faster than by numerical diagonalization and saved considerable computer time. The potentials, $V_{\mathrm{Ar}_n\mathrm{X}}$, are then referred to their own asymptotes by adding $\frac{1}{3}\Delta$ to the X and I state potentials, and subtracting $\frac{2}{3}\Delta$ from the II state potential. The total potential of the cluster is then obtained by adding the Ar–Ar potentials in a pairwise fashion. The well depths are found by minimizing these potentials using the simulated annealing and gradient minimization procedures described in Sec. IV B. For the X state, for example,

$$\epsilon_X = \min(V_{\mathrm{Ar}_n\mathrm{X}} + V_{\mathrm{ArAr}}), \tag{17}$$

with V_{ArAr} the same as in Eq. (11).

There are several assumptions implicit in this treatment of the open-shell potentials. First, the basis set is limited to p orbitals; excited orbitals of the halogen or rare gas atoms are not included. Thus, many-body effects due to polarization of the halogen atom or charge transfer are neglected. Also, we assume that the spin–orbit constant Δ is independent of the internuclear separations, as well as independent of the number of rare gas atoms in the cluster. To verify the former assumption, Δ was calculated as a function of R for ArBr and ArI, using the relations given by Haberland[24] and Aquilanti *et al.*,[38] and the three diatomic potential energy curves determined from the ZEKE spectra. The calculated Δ does not vary more than 1 meV (0.1%) for ArI and not by more

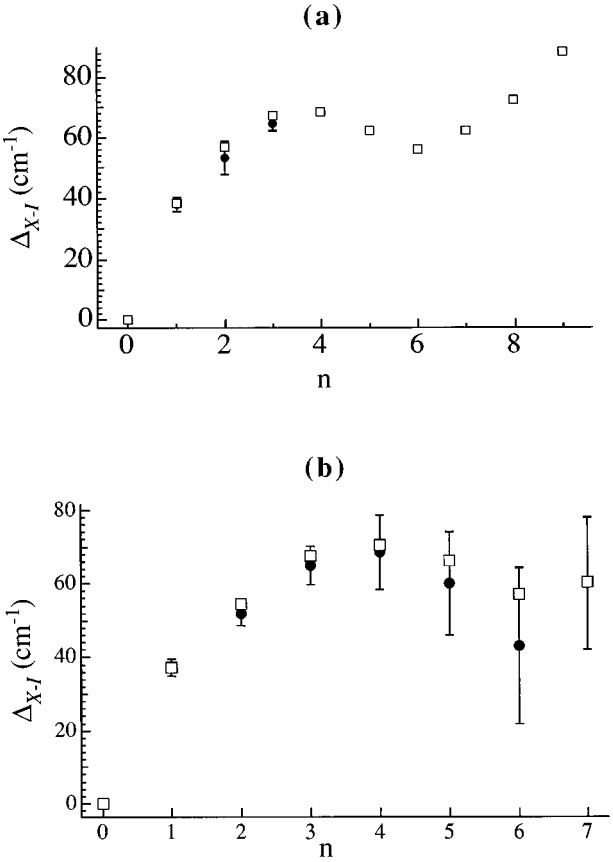

FIG. 8. Comparison of experimental and calculated $X-I$ state splittings for (a) Ar_nBr and (b) Ar_nI. Solid circles: experimental. Open squares: calculated as described in Sec. IV E.

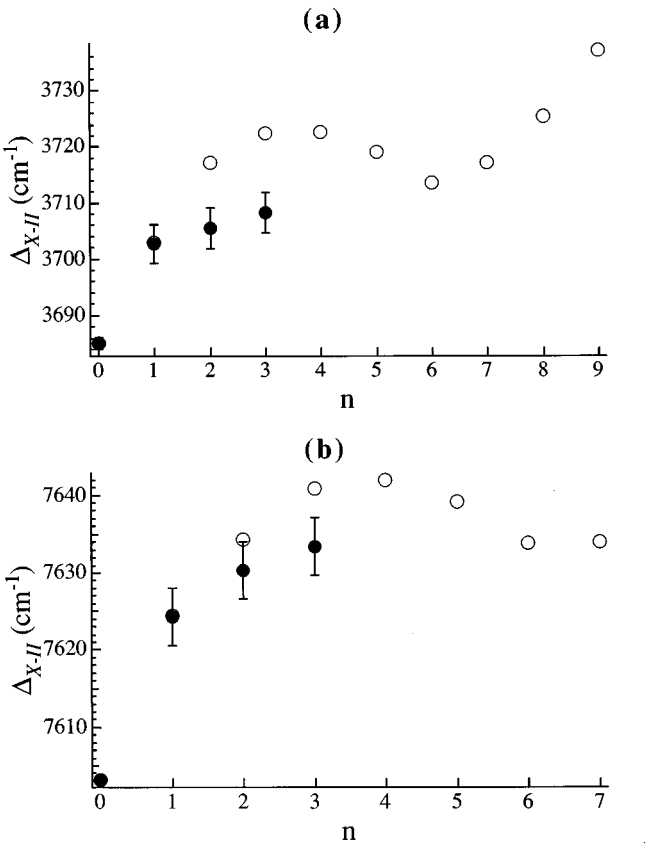

FIG. 9. Comparison of experimental and calculated $X-II$ state splittings for (a) Ar_nBr and (b) Ar_nI. Solid circles: experimental. Open circles: calculated as described in Sec. IV E.

than 5 meV (1%) for ArBr for R greater than the zero crossing point. The assumption that Δ is independent of the number of argon atoms is more questionable, as we will see below.

The above method of calculating the adiabatic potential surfaces was used directly in the simulated annealing procedure for the smaller clusters ($n \geqslant 6$). For the larger clusters, the annealing was first performed using the anion potentials described above, and then the system was allowed to relax (to optimize the geometry) on each of the neutral surfaces. In most cases, the anion and neutral have approximately the same global minimum configurations. There are some exceptions. For instance, the global minimum isomer of the Ar_5Br^- anion has all five of the Ar atoms in contact with the Br^- atom, but this geometry corresponds to a local minimum of the neutral X state surface. In such cases, the neutral minimum corresponding to the anion global minimum was always used to compute the ''adiabatic'' EAs and neutral electronic state splittings.

The results of the calculation of the neutral binding energies, zero point energies, Δ_{X-I}, and Δ_{X-II} are presented in Tables IV and V, for $Ar_{2-9}Br$ and $Ar_{2-19}I$, respectively. It is interesting to note that for all $n>1$, the zero point energy of the I state is greater than that of the X state, contrary to intuition. This seems to be due to the steep repulsive wall of the $I\frac{1}{2}$ diatomic state, which causes the antisymmetric modes to be more steeply curved in the I than in the X state. The result is an increase in Δ_{X-I} over what would be calculated if the zero point energies were neglected.

We can compare the $X-I$ splittings calculated using Eq. (3) with the experimental results without reference to the anion potential. This comparison is shown in Fig. 8. In the cases where the two states are well resolved, the agreement with experiment is quite satisfactory.

For $n=2$ and 3 the splitting between the X and II states may also be compared with experiment using Eq. (4), as shown in Fig. 9. For both $Ar_{2-3}Br$ [Fig. 9(a)] and $Ar_{2-3}I$ [Fig. 9(b)], the theoretical Δ_{X-II} is greater than the experimental value by about 5–15 cm^{-1}. The agreement is somewhat worse for $Ar_{2-3}Br$ than for $Ar_{2-3}I$. This discrepancy could mean that the atomic spin–orbit splitting Δ is not independent of the number of Ar atoms, as was assumed above. It is known that the spin–orbit splitting of atoms in rare gas matrices is different from that of the free atoms. For example, Lawrence and Apkarian found that the I atom spin–orbit splitting is decreased by about 3% or 5% in Xe or Kr matrices, respectively.[37] We observe a smaller decrease of Δ in the small clusters studied here: about 0.06–0.1 % in $Ar_{2-3}I$ and 0.3–0.4 % in $Ar_{2-3}Br$.

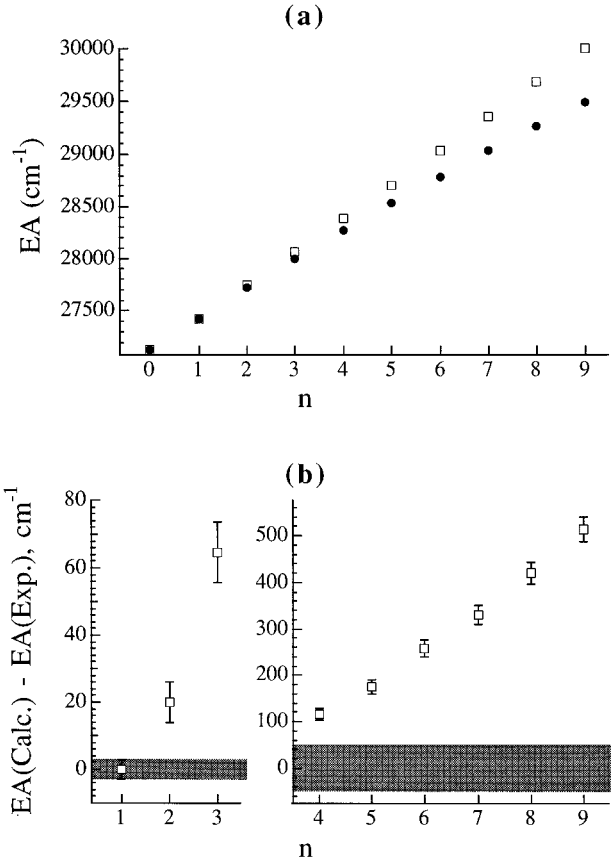

FIG. 10. Comparison of experimental Ar_nBr electron affinities (EAs) with those calculated from the pairwise additive model. (a) EA as a function of n. Solid circles: experimental EAs. Open squares: additive calculation. (b) Difference between calculated and experimental EAs as a function of n. The shaded region represents the experimental uncertainty. The error bars represent the uncertainty in the calculated EAs.

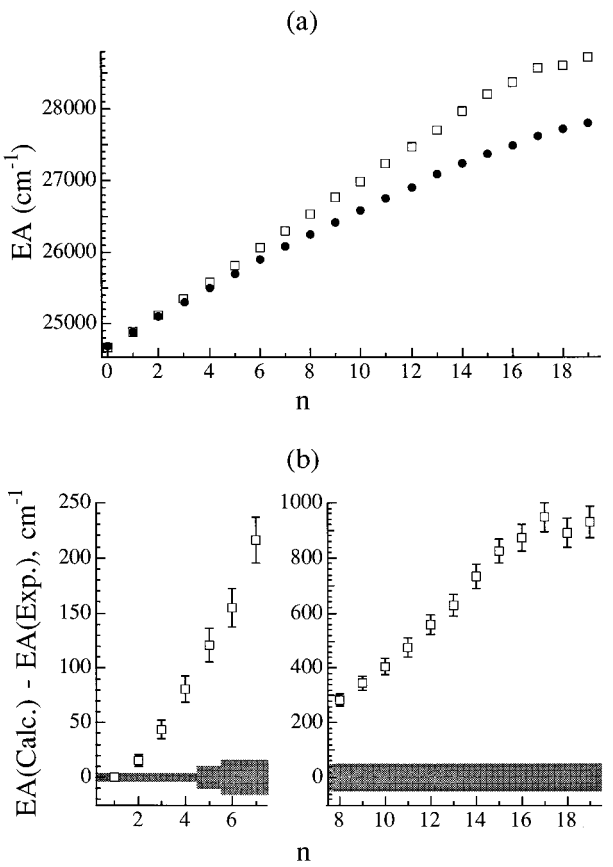

FIG. 11. Comparison of experimental Ar_nI EAs with those calculated from the pairwise additive model. (a) EA as a function of n. Solid circles: experimental EAs. Open squares: additive calculation. (b) Difference between calculated and experimental EAs plotted as a function of n. The shaded region represents the experimental uncertainty. The error bars represent the uncertainties in the calculated EAs.

Generally speaking, the open-shell interactions described in this section are nonadditive, in the sense that they are of the form of the additional terms in Eq. (2). However, they are not true many-body effects because they can be obtained directly from the pair potentials, and do not introduce additional interactions between the Ar atoms in contrast to the effects described in Sec. IV G. As pointed out by Sando and co-workers,[42] the open-shell potentials in the $n>1$ clusters can be considered to be additive as matrices rather than as scalars, and we will refer to these interactions as ''matrix additive'' effects in the rest of this discussion.

F. Electron affinities calculated from additive potentials

The adiabatic EAs calculated from Eq. (5) using the additive anion potentials [Eq. (11)] and ''matrix additive'' neutral potentials [Eq. (17)] are given in Tables IV and V. These are compared with the experimental EAs in Fig. 10 and 11. First, notice that in both $Ar_{2-9}Br$ and $Ar_{2-19}I$ the calculated EAs are significantly larger than the experimental results. For $Ar_{17-19}I$, the calculated EAs are almost 1000 cm^{-1} larger than the experimental values. Furthermore, the calculated EAs for $n\leqslant 17$ are nearly linear as a function of n. There is a slight positive curvature due to the nonadditivity of the neutral X state, and for $n>17$ the plot becomes flat in the case of Ar_nI^-. On the other hand, the experimental EAs display a significant negative curvature when plotted versus n. In Ar_nI, flattening out at $n=17$ is not observed. Clearly the model potentials, as described so far, are not consistent with experiment.

Before we consider many-body effects in the anion, let us first rule out other possible explanations for this inconsistency. We first consider the propagation of the uncertainties in the pair potentials. The theoretical error bars shown in Fig. 10(b) and 11(b) were estimated by assuming an uncertainty of ± 3 cm^{-1} in the quantity $\epsilon_a-\epsilon_x$ for the pair potentials, as discussed above, and multiplying this by the number of Ar–X nearest neighbors. The uncertainty in the Ar–Ar potential, and that due to ''relaxation'' of the geometry is neglected. The shaded areas in the figures represent the experimental uncertainties. The theoretical and experimental uncertainty regions show no overlap for $n>2$. If a much more conservative estimate of the uncertainties is desired, we can consider the individual uncertainties in the diatomic well

depths, i.e., 9 cm^{-1} for ArBr and $ArBr^-$, and 18 cm^{-1} for ArI and ArI^-. Even in this case, the experimental and theoretical error ranges overlap only for Ar_2Br and $Ar_{2-3}I$.

Furthermore, because the trends in the size dependence of the observed EAs are so different from those of the calculated EAs, it does not seem possible to modify the pair potentials so as to simultaneously account for all the experimental EAs. Any modification of the pair potentials would result in the same more or less linear trend in theoretical EAs.

One might also ask whether the population of local minima affects the trends in the experimental EAs. We can rule this out for $Ar_{2-3}X$, for which there is only one possible minimum geometry. For $n=4$ and 5 the only local minima give calculated EAs much lower than the experimental result. For some of the larger clusters there may be local minima that would be consistent with the experimental EAs. However, we know from the diatomic spectra[4] that the vibrational temperatures in the molecular beam are on the order of 50 K. In light of this, a significant population of larger clusters occupying local minima several hundred cm^{-1} above the global minimum seems unlikely. For this reason, and because it is not possible to account for the observed EAs of the small clusters with alternate minima, it is very unlikely that population of local minima could be the sole explanation for the observed trends in the EAs.

Next we consider various nonadditive terms in the potentials.

G. Many-body interactions

Nonadditive (or many-body) interactions fall into three categories: those present in both the anion and the neutral, those unique to the neutral, and those unique to the anion. Many-body interactions present in both anion and neutral include dispersion (Axilrod–Teller) and exchange interactions. Interactions unique to the neutral include the ''many-body'' effects due to the open-shell nature of the halogen atom, which have already been discussed in Sec. IV E. Many-body effects unique to the anion are those involving the charge on the halide atom. These include nonadditive induction effects, and the interaction of the halide charge with multipole moments caused by exchange and dispersion interactions between pairs of argon atoms.

The experimental observable, the EA, depends on the difference between the anion and neutral potentials [see Eq. (5)], and is therefore most sensitive to many-body effects that occur in the anion or neutral but not both. The following discussion will show that many-body effects unique to the anion have the largest effect on the trends in electron affinities.

We will consider each nonadditive effect in turn, incorporating it into our simulated annealing procedure to test its effect on cluster energetics at the minimum energy geometry.

1. Triple-dipole interaction

The leading term in the nonadditive dispersion energy, the triple-dipole interaction, was first derived by Axilrod and Teller,[46] and independently by Muto.[47] The form of the triple-dipole potential is, for three atoms i, j, and k,

$$V_{ddd}=C_9\,\frac{(3\cos\theta_i\cos\theta_j\cos\theta_k+1)}{R_{ij}^3R_{jk}^3R_{ik}^3}, \tag{18}$$

where θ_i is the interior angle $\angle jik$, R_{ij} is the internuclear distance between atom i and atom j, and C_9 is a constant depending only on the identities of the three atoms. C_9 can be calculated using semiempirical methods[48] or by fitting to *ab initio* calculations.[49] However, because such results are not available for the Ar_nX or Ar_n^- systems considered here, we use the approximation to C_9 discussed by various authors,[48(b),50]

$$C_9=\tfrac{3}{2}\alpha_i\alpha_j\alpha_k\,\frac{\eta_i\eta_j\eta_k(\eta_i+\eta_j+\eta_k)}{(\eta_i+\eta_j)(\eta_j+\eta_k)(\eta_i+\eta_k)}, \tag{19}$$

where α_i and η_i are, respectively, the dipole polarizability and average excitation energy of atom i.

A simple approximation to η_i is, in atomic units,[50,51]

$$\eta_i=\left(\frac{N_i}{\alpha_i}\right)^{1/2}. \tag{20}$$

Here N_i is an effective number of electrons for a given atom. Substituting Eq. (20) into Eq. (19) gives a three-body analogue of the Slater–Kirkwood formula[51] for the C_6 dispersion coefficient. In the treatment of Koutselos and Mason,[50(a)] which we follow here, N_i is treated as an empirical parameter determined from the corresponding C_6 two-body dispersion coefficient for like atoms. Furthermore, the values of N_i for the halide anions for which the C_6 coefficients are not known are assumed to be the same as those of the corresponding isoelectronic rare gases. Some theoretical and empirical justification of the approximations involved in this approach is given by Koutselos and Mason, who estimate an uncertainty of 5%–10 % for C_9 coefficients determined in this way.[50(a)] The parameters N and α as well as the values of C_9 calculated from Eqs. (19) and (20) are given in

TABLE VI. Atomic dipole and quadrupole polarizabilities, effective numbers of electrons, and C_9 coefficients for Ar–Ar–X interactions.

Atom	α (a_0^3)	C (a_0^5)	N	C_9 (eV Å^9)
Ar	11.08[a]	27.11[d]	5.90[e]	⋯
Br^-	35.2[b]	164[d]	6.70[e]	127
Br	20.6[c]	⋯	6.2[e]	83
I^-	52.7[b]	254[d]	7.79[e]	179
I	36.1[c]	⋯	6.5[e]	129

[a]R. R. Teachout ad R. T Pack, At. Data **3**, 195 (1971).
[b]H. Coker, J. Phys. Chem. **80**, 2078 (1976).
[c]*Handbook of Chemistry and Physics*, 74th ed. (CRC, Boca Raton, 1994), pp. 10–198.
[d]M. V. K. Sastri, P. L. Narasimhulu, and K. D. Sen, J. Chem. Phys. **80**, 584 (1984). Note that we use Buckingham's definition [Adv. Chem. Phys. **12**, 107 (1967)] of the quadrupole polarizability C, which is equal to half of the quadrupole polarizability, α_q, used by Sastri *et al.* [See E. A. Gislason and M. S. Rajan, Chem. Phys. Lett. **50**, 251 (1977) and references therein for information on the various quadrupole polarizability conventions.]
[e]E. A. Mason and E. W. McDaniel, *Transport Properties of Ions in Gases* (Wiley, New York, 1988), pp. 533–534.

Table VI. It should be noted that Eqs. (18) and (19) are, strictly speaking, valid only for atoms in S states.[46(b),50(a)] In extending their use to P-state halogens we are implicitly neglecting the anisotropy of the halogen atom polarizability.

The triple-dipole interaction is repulsive for near equilateral geometries. In the case of Ar_2I^-, V_{ddd} at the equilibrium geometry is $+8.1$ cm^{-1}, and 6.3 cm^{-1} for Ar_2I. For Ar_2Br^- and Ar_2Br, the results are 9.0 and 5.7 cm^{-1}, respectively. The larger values for the anionic clusters are mainly due to their greater polarizabilities. The net result, then, is a decrease in the calculated EA by about 2–3 cm^{-1} compared with the additive potentials. This effect is of the same order as the experimental uncertainty, but may be more significant for larger clusters. In the calculations below on clusters with $n \geqslant 3$, only the Ar–Ar–X triple-dipole interactions are included. The Ar–Ar–Ar interactions are neglected, because we expect their energies to be nearly equal in the anion and neutral.

It has been shown that higher-multipole three-body dispersion terms, such as the dipole–dipole–quadrupole (V_{ddq}) potential, may also contribute substantially to the three-body dispersion energy.[2] To ascertain their importance here, we used the formulas of Koutselos and Mason[50(a)] for the higher multipole coefficients, and the geometrical factors given by Bell[52] to estimate V_{ddq} for Ar_2I^- and Ar_2I. At the equilibrium geometries of the clusters determined with additive potentials, we obtain approximately 4 cm^{-1} for Ar_2I^- and 3 cm^{-1} for Ar_2I. The resulting 1 cm^{-1} shift in the EA is smaller than the experimental uncertainty. Therefore, V_{ddq} and all higher multipole three-body dispersion terms were neglected in subsequent calculations.

2. Three-body exchange

The second type of three-body interaction that occurs in both anion and neutral clusters is the three-body exchange interaction. This is caused by the exchange induced electron charge distortion of a pair of atoms, which alters the pair's exchange interaction with a third atom. This effect is difficult to model without recourse to *ab initio* calculations, and has been the subject of some controversy.[2,3] As far as we are aware, such calculations are not available for the Ar_nBr/Ar_nBr^- or Ar_nI/Ar_nI^- systems studied here. However, we can get an idea of the magnitude of this effect from an *ab initio* calculation on Ar_3 by Chalasinski, Szczesniak, and Cybulski.[49] For equilateral Ar_3 at internuclear separations close to the equilibrium Ar_2 bond length, they find the sum of first and second order exchange three-body energies to be -1.5 cm^{-1}, or about 42% of the third order dispersion nonadditive energy ($+3.6$ cm^{-1}), and of opposite sign. If we assume the exchange nonadditivity is a similar percentage of the dispersion nonadditivity in the Ar_nBr/Ar_nBr^- and Ar_nI/Ar_nI^- systems, we would anticipate a 2–4 cm^{-1} negative contribution to the binding energies, and an approximately 1 cm^{-1} difference between anion and neutral three-body exchange energies. Because this effect is expected to be small compared with our experimental uncertainties, and due to the practical difficulty of accurately modeling it, it will be neglected here.

3. Induction nonadditivity

The anion pair potentials are dominated by induction. Likewise, we expect a rather large nonadditive effect to arise from the interaction between multipole moments induced in the rare gas atoms by the halide charge. In addition, there is nonadditivity due to the polarization of the halide atom itself. Because these effects are entirely absent in the neutral clusters (if we neglect the relatively small inductive effects due to the permanent quadrupole moment of the neutral halogen), we expect the induction nonadditivity to have a large effect on the EA.

A model for treating nonadditive effects in systems of polarizable particles, first developed by Vesely,[53] has been extended and used extensively by various workers in computer simulations of solvated ions[54] and electrons,[55] polar liquids,[56] and ionic clusters.[18,56(d),57] Our adaptation of this model is as follows.

Each atom is characterized by a point charge (halide only) and point dipole and quadrupole polarizabilities (halide and rare gases) located at the nucleus. We assume that the induced dipole of an atom depends linearly on the electric field produced by the charges and multipoles of the other atoms via the dipole polarizability α. We neglect the cubic dependence on the electric field due to the hyperpolarizability γ and all higher terms. Likewise, we consider only quadrupoles induced by the field gradient due to the other atoms, characterized by the quadrupole polarizability C, neglecting the smaller contribution quadratic in the electric field via the dipole–quadrupole hyperpolarizability B,[58] and higher terms.

We also neglect the damping of the polarizabilities and charges at short range due to exchange or charge transfer. Such effects are believed to be significant in the case of hydrogen bonding[56(a)] and in anions in ionic crystals.[59] However, they are probably less important in the weakly bound clusters considered here.

With these assumptions, the electric field at atom i is given by[60]

$$E_\alpha^{(i)} = \sum_{j \neq i} \left(-T_\alpha^{(ij)} q_j + T_{\alpha\beta}^{(ij)} \mu_\beta^{(j)} - \tfrac{1}{3} T_{\alpha\beta\gamma}^{(ij)} \Theta_{\beta\gamma}^{(j)} \right), \tag{21}$$

and the electric field gradient is[60]

$$E_{\alpha\beta}^{(i)} = \sum_{j \neq i} \left(-T_{\alpha\beta}^{(ij)} q_j + T_{\alpha\beta\gamma}^{(ij)} \mu_\gamma^{(j)} - \tfrac{1}{3} T_{\alpha\beta\gamma\delta}^{(ij)} \Theta_{\gamma\delta}^{(j)} \right). \tag{22}$$

Here, following the notation of Buckingham,[60] the subscripts α, β, γ, and δ stand for any of the Cartesian components of a vector or tensor, and repeated Greek subscripts imply summation over the three components. The permanent electric charge is represented by q_i (-1 for the halide and 0 for the rare gases), and $\mu_\alpha^{(i)}$ and $\Theta_{\alpha\beta}^{(i)}$ are components of the induced dipole and quadrupole moments, respectively, at atom i. We use Buckingham's definition of the quadrupole moment as a traceless tensor.[60] The multipole interaction tensors are de-

fined by $T^{(ij)}_{\alpha\beta\cdots v}=\nabla_\alpha\nabla_\beta\cdots\nabla_v(1/R_{ij})$, where $\mathbf{R}_{ij}$ is the vector from atom j to atom i. The induced dipole at atom i is then given by[60]

$$\mu^{(i)}_\alpha=\alpha_i E^{(i)}_\alpha, \tag{23}$$

and the induced quadrupole is[60]

$$\Theta^{(i)}_{\alpha\beta}=C_i E^{(i)}_{\alpha\beta}, \tag{24}$$

where α_i and C_i are the dipole and quadrupole polarizabilities, respectively, of atom i. The values of α and C used here are given in Table VI.

At each time step in the simulated annealing procedure, the induced moments are calculated iteratively from Eqs. (21)–(24). At the first time step, the field and field gradient due to the halide permanent charge are initially calculated from Eqs. (21) and (22). Then the induced moments are found from Eqs. (23) and (24), and substituted back into Eqs. (21) and (22). The process is repeated until the magnitudes of the induced moments do not change by more than one part in 10^{-10} with successive iterations. It is found that the moments converge about twice as fast if the individual moments are immediately substituted into Eqs. (21) and (22) for subsequent calculations during a given iteration, rather than ''saved'' until the next iteration. For subsequent molecular dynamics (MD) time steps, the algorithm is initiated with the induced moments saved from the previous MD step. This saves some computer time.

The total induction energy is then given by

$$V_{\text{ind,total}}=V_{q\mu}+V_{q\Theta}+V_{\mu\mu}+V_{\mu\Theta}+V_{\Theta\Theta}+V_{\text{self}}, \tag{25}$$

where the first five terms on the right-hand side are the charge–dipole, charge-quadrupole, dipole–dipole, dipole–quadrupole and quadrupole–quadrupole interaction energies. The final term is the energy required to create the induced dipoles and quadrupoles, given by[61,62]

$$V_{\text{self}}=\sum_i\left(\frac{\mu^{(i)}_\alpha\mu^{(i)}_\alpha}{2\alpha_i}+\frac{\Theta^{(i)}_{\alpha\beta}\Theta^{(i)}_{\alpha\beta}}{6C_i}\right), \tag{26}$$

where the sum runs over all atoms. By using Eqs. (21)–(24) for one of each of the dipoles and quadrupoles in Eq. (26) and substituting the explicit expressions for the interaction energies[60] and Eq. (26) into Eq. (25), one can show that Eq. (25) simplifies to

$$V_{\text{ind,total}}=\tfrac{1}{2}V_{q\mu}+\tfrac{1}{2}V_{q\Theta}=\sum_i\sum_{j\neq i}q_i\left(-\tfrac{1}{2}T^{(ij)}_\alpha\mu^{(j)}_\alpha+\tfrac{1}{6}T^{(ij)}_{\alpha\beta}\Theta^{(j)}_{\alpha\beta}\right). \tag{27}$$

This equation gives the total induction energy of the cluster. However, part of this energy is already implicitly included in the $Ar–X^-$ pair potential. In order to extract the nonadditive portion, we calculate the induction energy for each $Ar–X^-$ pair, neglecting the other Ar atoms in the cluster, using the same iterative method. The sum of the pair induction energies is then subtracted from Eq. (27) to give the nonadditive induction energy:

$$V_{\text{ind}}=V_{\text{ind,total}}-V_{\text{ind,pair}}. \tag{28}$$

In practice, due to the computational ''expense'' of this iterative calculation, a simpler model was employed for the initial simulated annealing procedure. In the simpler model, the interaction energy between dipoles directly induced in the rare gas atoms by the halide charges is calculated.[63] The minimum energy geometries found with the simpler model were then optimized using the full iteratively calculated induction model described above.

The results of the calculation for Ar_2I^- and Ar_2Br^- show that the nonadditive induction effect is indeed quite large. For Ar_2Br^-, for example, V_{ind} is 35.3 cm^{-1}. The result for Ar_2I^- is somewhat smaller, because of the larger $Ar–X^-$ internuclear distance. The nonadditive induction energy is always found to be positive, showing that it is dominated by the repulsion between adjacent induced multipoles on the Ar atoms. The dipole term of Eq. (27) contributes 32.7 cm^{-1} to the total in Ar_2Br^-, and the quadrupole term contributes 2.6 cm^{-1}. Thus, it does appear necessary to include the induced quadrupole effect, usually neglected in this type of simulation, for accurate calculation of the binding energies. The results for the larger clusters are discussed below.

4. Exchange and dispersion multipoles

As first described by Dick and Overhauser,[64] the exchange repulsion between two closed-shell atoms produces a buildup of negative charge near the nuclei and a depletion of electron density between the nuclei. At large distances from the pair of atoms this distortion of the electron clouds is equivalent to a set of multipole moments, as discussed by Jansen.[65] If the atoms are identical, the first nonvanishing moment is a quadrupole. There is also a quadrupole, of opposite sign, arising from the dispersion interaction between two atoms. At the usual van der Waals distances, the dispersion contribution is somewhat smaller than the exchange contribution.[66]

In the case of Ar_nBr^- and Ar_nI^-, a three-body effect then arises from the interaction of the halide charge with the Ar_2 exchange/dispersion multipoles. This is another type of many-body interaction that is present in the anionic but not in the neutral clusters, and is therefore expected to have a significant effect on the EA. As with induction, we expect the interaction of the permanent quadrupole of the neutral halogen atom with the exchange/dispersion moments to be negligible.

In their studies of the Ar_2–HCl, –DCl, and –HF systems, Hutson and coworkers[10] have found that the interaction of the exchange/dispersion quadrupole of the Ar_2 unit with the permanent multipoles of the HX molecule is quite important. This work was mainly concerned with the interpretation of the vibration–rotation spectra[7,8] of the clusters. However, they also found the contribution to the binding energy to be significant. Chalasinski and others[67] have found these conclusions about the importance of the exchange quadrupole effect on the Ar_2HX potential energy surfaces to be qualitatively consistent with their *ab initio* calculations. In recent work more closely related to our own, Burcl *et al.* have extracted information about the exchange multipole energy

from *ab initio* calculations on Ar_2Cl^-.[68] These authors calculated this effect to be -12.8 cm^{-1} near the equilibrium geometry of Ar_2Cl^-. In this light we expect the exchange/dispersion multipole contribution to the nonadditive binding energies of our Ar_nBr^- and Ar_nI^- clusters also to be quite significant.

Jansen derived a simple expression for the exchange quadrupole using an effective one electron model for the atomic charge distributions.[65] In this approach, the electronic charge density of an atom is approximated by a single Gaussian function,

$$\rho_i(\mathbf{r}) = -\frac{|e|\beta^3}{\pi^{3/2}} e^{-\beta^2|\mathbf{R}_i-\mathbf{r}|^2}, \tag{29}$$

where β is the Gaussian range parameter, $\mathbf{R}_i$ is the position of the nucleus of atom i, and $\mathbf{r}$ is the position of the effective electron. Then the atomic wave function is defined as

$$\varphi_i(\mathbf{r}) = \left|\frac{\rho_i(\mathbf{r})}{e}\right|^{1/2}. \tag{30}$$

The zero-order wave function of a pair of atoms, i and j, is taken to be the antisymmetrized product of the two atomic wavefunctions (normalized to 2):

$$\Psi^0_{ij}(\mathbf{r},\mathbf{r}') = \frac{1}{(1-S^2_{ij})^{1/2}}[\varphi_i(\mathbf{r})\varphi_j(\mathbf{r}') - \varphi_i(\mathbf{r}')\varphi_j(\mathbf{r})]. \tag{31}$$

Here $\mathbf{r}$ and $\mathbf{r}'$ are the positions of the two electrons, and S_{ij} is the overlap integral, which for like atoms with Gaussian wave functions is given by

$$S^2_{ij} = \exp(-\beta^2 R^2_{ij}/2),$$

where R_{ij} is the internuclear separation between the atoms. Then, taking the expectation value of the quadrupole moment operator with wave function (31), a simple expression for the cylindrically symmetric exchange quadrupole is found:[65]

$$\Theta_{ex}(R_{ij}) = -\frac{|e|R^2_{ij}}{2}\left(\frac{S^2_{ij}}{1-S^2_{ij}}\right). \tag{32}$$

In Jansen's original treatment, the range parameter β was estimated from the long range dispersion interactions, and assumed to be valid for short range exchange interactions. This method of estimating β is now believed to significantly overestimate the exchange quadrupole.[69,70] An approach that has been used to improve the accuracy of the model is to fit the one-electron functional form for the exchange quadrupole to the results of accurate *ab initio* calculations, to arrive at a more reasonable value of β.[10,69] Here, we shall use the value $\beta = 0.936$ Å^{-1}, derived in this way by Hutson and co-workers[10(c)] from a self-consistent field (SCF) calculation of the quadrupole moment of Ar_2.

The problem now arises of how to calculate the interaction energy of the exchange quadrupole with the halide charge. The simplest way is to represent the exchange charge distribution with a point quadrupole, calculated from Eq. (32), located at the midpoint between the two Ar atoms. The energy is then obtained from the standard expression for a charge–quadrupole interaction.[60] However, because the typical halide–Ar_2 distances in the clusters are on the same order as the Ar–Ar distance, the point quadrupole representation overestimates the magnitude of the interaction. The point quadrupole representation was used by Hutson *et al.* in their work on Ar_2–HCl and –DCl, and was found by them to somewhat overcorrect the pairwise additive potential.[10(a),10(b)] In more recent work on Ar_2–HF, Ernesti and Hutson[10(c)] proposed a distributed dipole representation: The Ar_2 exchange charge distribution is represented by opposed point dipole moments at the two Ar nuclei, parallel to the internuclear axis, with magnitudes chosen to give the same overall quadrupole moment as Eq. (32). Ernesti and Hutson found the distributed dipole representation superior to the point quadrupole representation for Ar_2–HF, but noted that it somewhat underestimated the electric field of the true charge distribution.[10(c)]

The difficulty with both of these approaches arises from the use of a multipole representation at short range. Therefore, it seems logical to attempt a more direct calculation of the interaction of the exchange charge distribution with the halide charge. To do this, we form an effective charge density—the part of the charge density that contributes to the exchange quadrupole—by subtracting the atomic charge densities (29) from the charge density of the antisymmetrized wave function (31):

$$\begin{aligned}\rho_{\text{eff}}(r) &= -|e|\int |\Psi^0_{ij}(\mathbf{r},\mathbf{r}')|^2 d\mathbf{r}' - \rho_i(\mathbf{r}) - \rho_j(\mathbf{r}) \\ &= -\frac{|e|S^2_{ij}}{1-S^2_{ij}}\left(\frac{\beta}{\pi^{1/2}}\right)^3 [e^{-\beta^2|\mathbf{R}_i-\mathbf{r}|^2} + e^{-\beta^2|\mathbf{R}_j-\mathbf{r}|^2} \\ &\quad - 2e^{-\beta^2|\mathbf{R}_C-\mathbf{r}|^2}].\end{aligned} \tag{33}$$

Here $\mathbf{R}_C = \frac{1}{2}(\mathbf{R}_i + \mathbf{R}_j)$ is the midpoint between the two Ar nuclei. We see that the effective charge density is the sum of two negative Gaussian charge distributions located at the nuclei, and a positive Gaussian distribution, twice as large, at $\mathbf{R}_C$.[64] If we approximate the halide with a point charge at $\mathbf{R}_0$, the Coulomb interaction energy is then found to be[71]

$$\begin{aligned}V_{\text{ec}} = \sum_{i<j} \frac{e^2 S^2_{ij}}{1-S^2_{ij}}\Bigg[&\frac{\text{erf}(\beta R_{i0})}{R_{i0}} + \frac{\text{erf}(\beta R_{j0})}{R_{j0}} \\ &- 2\frac{\text{erf}(\beta R_{C0})}{R_{C0}}\Bigg],\end{aligned} \tag{34}$$

where R_{i0}, R_{j0}, and R_{C0} are the distances of the halide from the Ar nuclei and the midpoint between the nuclei, respectively, and i and j run over the Ar atoms. The error functions in Eq. (34) can be easily evaluated using standard subroutines.[72] In the limit $\beta R \to \infty$, $\text{erf}(\beta R) \to 1$. So at long range, Eq. (34) is equivalent to the Coulomb interaction of the halide charge with negative point charges $\delta = -|e|S^2_{ij}/(1-S^2_{ij})$ at the Ar nuclei, and a positive point charge, $+2|\delta|$, at $\mathbf{R}_C$.[65] In order to prevent nonphysical be-

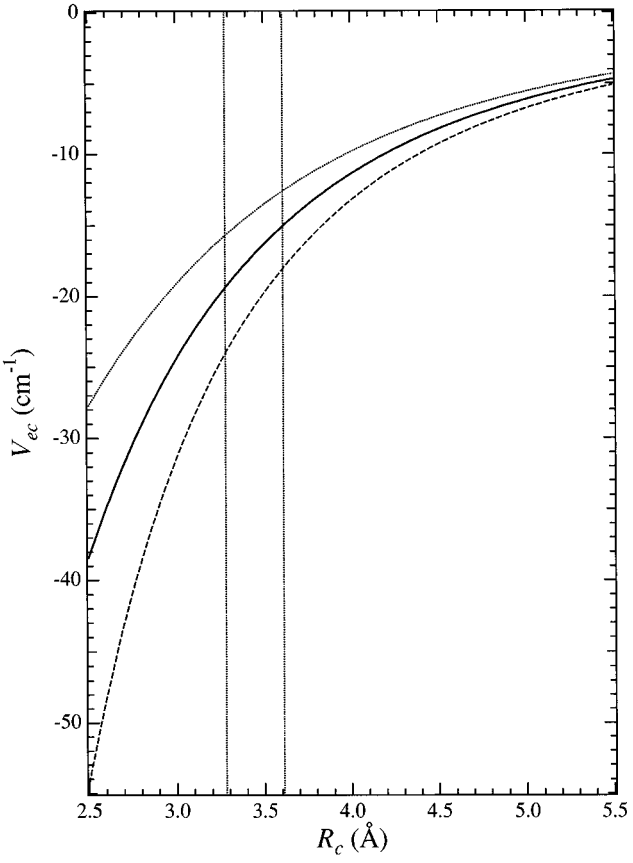

FIG. 12. Comparison of three models of the exchange quadrupole–charge interaction in Ar_2X^- clusters. The Gaussian range parameter β is 0.936 Å, and the Ar–Ar distance is fixed at 3.7565 Å. R_c is the distance between the halide nucleus and the Ar–Ar midpoint. Dashed line: point quadrupole model. Dotted line: distributed dipole model. Solid line: calculated from Eq. (34). The vertical lines represent the Ar–Br^- and Ar–I^- dimer equilibrium distances.

havior of Eq. (34) for small values of R_{C0} (near linear geometries), $V_{\rm ec}$ is cut off for Ar–Ar separations greater than a certain value, typically 6.5 Å.

We should discuss the approximations implicit in Eq. (34). First, the nuclear charges are, in effect, approximated by Gaussian distributions with the same β parameter as the atomic electron densities. Thus, effects of nuclear deshielding are not included in Eq. (34). Second, the approximation of the halide by a point charge will underestimate the extent of overlap effects and hence tend to slightly overestimate the magnitude of the interaction energy. This deficiency could be corrected if more were known about the charge densities of the halide atoms. Finally, and most importantly, we are still working within the Gaussian one-electron approximation. A single Gaussian function is known to be a rather poor approximation to the true electron density of an atom.[70] This problem could be overcome by using a more accurate model of the Ar_2 charge distribution, such as the result of an *ab initio* calculation with Gaussian type basis functions. The method of Gaussian multipoles developed by Wheatley[71] could then be used to calculate the Coulomb energy. Despite the limitations of the present model, we nonetheless expect Eq. (34) to give a more accurate value of $V_{\rm ec}$ than either the point quadrupole or distributed dipole representations.

The three models of $V_{\rm ec}$ are compared for Ar_2X^- in Fig. 12. In the figure, the Ar–Ar distance is held constant at the equilibrium value of the Ar_2 molecule, and the Ar–Ar axis is kept perpendicular to $\mathbf{R}_{C0}$, as the halide–Ar_2 distance is varied. It can be seen that at large separations, the three models approach each other, as expected. However, at separations near the equilibrium structures of Ar_2I^- and Ar_2Br^-, the differences among the three models are quite significant. For example, at $R_{C0}=3.61$ Å, corresponding to Ar_2I^-, Eq. (34) gives $V_{\rm ec}=-15.0$ cm^{-1}, compared with -18.0 cm^{-1} for the point quadrupole model, and -12.6 cm^{-1} for the distributed dipole representation. The differences among the three models at the equilibrium R_{C0} of Ar_2Br^- (3.28 Å) are even more pronounced. We conclude that at the interatomic distances considered here, it is important to use an accurate representation of the exchange charge distribution to calculate $V_{\rm ec}$. In the remainder of this work, we shall use Eq. (34) for $V_{\rm ec}$.

We also need to consider the multipole moments induced in the rare gas atoms by dispersion. Hunt[73] has developed a model for the dispersion induced dipole and quadrupole moments in terms of atomic polarizabilities and dispersion coefficients. The average dipole moment induced on atom i by the dispersion interaction with other like atoms is given by

$$\mu^{i,\rm disp}=C_\mu\sum_{j\neq i}\frac{\hat{\mathbf{R}}_{ij}}{R_{ij}^7},\quad \text{with}\ C_\mu=\frac{3}{2}\frac{C_6B}{\alpha},\tag{35}$$

where $\hat{\mathbf{R}}_{ij}$ is the unit vector pointing from atom j to atom i, C_6 is the Ar–Ar dispersion coefficient, α is the dipole polarizability, and B is the dipole–quadrupole hyperpolarizability. The components of the dispersion induced quadrupole moment on atom i are given by

$$\Theta_{\alpha\beta}^{i,\rm disp}=-C_\Theta\sum_{j\neq i}\frac{T_{\alpha\beta}^{(ij)}}{2R_{ij}^3},\quad \text{with}\ C_\Theta=\frac{1}{4}\frac{C_6B}{\alpha},\tag{36}$$

where $T_{\alpha\beta}^{(ij)}=\nabla_\alpha\nabla_\beta(1/R_{ij})$. For example, in the special case of two atoms lying on the Z axis, the quadrupoles have cylindrical symmetry, with $\Theta_{zz}^{i,\rm disp}=-C_\Theta/R_{ij}^6$, and $\Theta_{xx}^{i,\rm disp}=\Theta_{yy}^{i,\rm disp}=-\frac{1}{2}\Theta_{zz}^{i,\rm disp}$. Following Ernesti and Hutson,[10(a)] the values of C_μ and C_Θ were found using the C_6 constant from the Aziz HFDID (Hartree–Fock dispersion individually damped) 1 potential,[29] and the ratio B/α from the calculation of Maroulis and Bishop.[74] We obtain $C_\mu=1252\ ea_0^8$ and $C_\Theta=208.6\ ea_0^8$. The total dispersion induced dipoles and quadrupoles are calculated from Eqs. (35) and (36) for each Ar atom. Then the charge–dipole interaction energy, $V_{d\rm dis}$ and the charge–quadrupole energy, $V_{q\rm dis}$, are computed from the standard electrostatic formulae.[60] We denote the total charge-dispersion multipole energy by $V_{m\rm dis}=V_{d\rm dis}+V_{q\rm dis}$.

We should note that this calculation is carried out independently of the nonadditive induction energy calculation described in the previous section (Sec. IV G 3). Therefore, interactions between the electrostatically induced multipoles and the exchange/dispersion induced multipoles have been

neglected. This is reasonable because the exchange/dispersion multipoles are about an order of magnitude smaller than the charge induced multipoles, and, therefore, the interactions of the exchange/dispersion multipoles with the charge are much larger than their interactions with the charge induced multipoles.

The charge–dipole energy, $V_{d\mathrm{dis}}$ is generally positive and about 30% as large as V_{ec}. This proportion is qualitatively consistent with the calculations of Lacey and Byers Brown[66] and with the results of Ernesti and Hutson.[10(c)] $V_{q\mathrm{dis}}$ is negative, and only about 5% as large as $V_{d\mathrm{dis}}$. For example, in Ar_2Br^-, the dispersion dipole energy is $+6.0$ cm^{-1}, and the dispersion quadrupole energy is -0.3 cm^{-1}. This may be compared with the exchange charge energy of -20.3 cm^{-1}. Thus we see that the dispersion dipole makes a nonnegligible contribution to the nonadditive energy, whereas the dispersion quadrupole could be neglected without any significant loss of accuracy.

Complete results for the larger clusters are discussed in the next section.

H. Electron affinities calculated with many-body potentials

In order to assess the importance of the various many-body effects mentioned above, we reoptimized the minimum energy geometries found from the simulated annealing procedure with the additive potentials, successively adding the many-body terms, in order of their relative magnitudes.

The first nonadditive term considered was the multipole induction energy; the anion potential was then found from

$$\epsilon_a = \min(V_{\mathrm{ArX}} + V_{\mathrm{ArAr}} + V_{\mathrm{ind}}), \tag{37}$$

where the right-hand terms are the pairwise additive argon–halide and argon–argon potentials, and the many-body multipole induction potential. The neutral potential was identical to that used in the calculation in Sec. IV E:

$$\epsilon_X = \min(V_{\mathrm{Ar}_n\mathrm{X}} + V_{\mathrm{ArAr}}), \tag{38}$$

where V_{Ar_nX} is the ''matrix additive'' X state potential described in Sec. IV E. We refer to the electron affinities calculated from Eqs. (37), (38), and (5) as $\mathrm{EA}_{\mathrm{ind}}$.

We next considered the effect of addition of the exchange–charge and multipole dispersion energies. The anion binding energies are then

$$\epsilon_a = \min(V_{\mathrm{ArX}} + V_{\mathrm{ArAr}} + V_{\mathrm{ind}} + V_{\mathrm{ec}} + V_{\mathrm{mdis}}), \tag{37'}$$

and the neutral binding energies are still given by Eq. (38). The electron affinities calculated from Eqs. (37′), (38), and (5) are referred to as $\mathrm{EA}_{\mathrm{ind+ec+}m\mathrm{dis}}$.

Finally, the Axilrod–Teller term was included in both the anion and neutral potentials to give

$$\epsilon_a = \min(V_{\mathrm{ArX}} + V_{\mathrm{ArAr}} + V_{\mathrm{ind}} + V_{\mathrm{ec}} + V_{\mathrm{mdis}} + V_{\mathrm{at}}^{\mathrm{anion}}), \tag{37''}$$

$$\epsilon_X = \min(V_{\mathrm{Ar}_n\mathrm{X}} + V_{\mathrm{ArAr}} + V_{\mathrm{at}}^{\mathrm{neutral}}). \tag{38'}$$

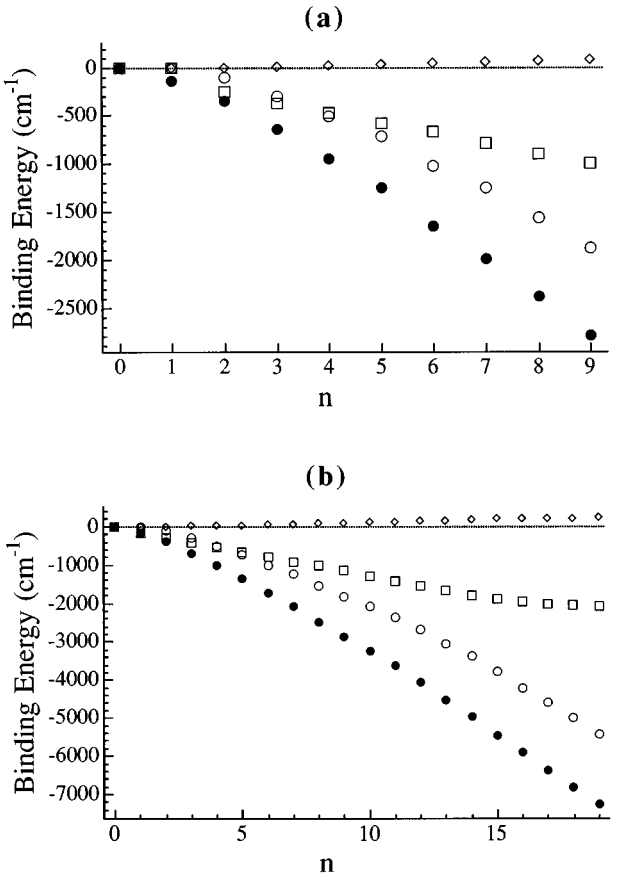

FIG. 13. Calculated contributions to the X state binding energies (BE) of (a) Ar_nBr and (b) Ar_nI neutral clusters. Solid circles: total BE. Open squares: Ar–Br contribution. Open circles: Ar–Ar contribution. Open diamonds: Axilrod–Teller triple-dipole contribution.

The EAs calculated from Eqs. (37″), (38′), and (5) are referred to as $\mathrm{EA}_{\mathrm{ind+ec+}m\mathrm{dis+at}}$. The binding energies calculated from Eqs. (37″) and (38′) and their components are shown graphically in Figs. 13 and 14.

The anion and neutral binding energies calculated from Eqs. (37), (37′), and (38), and from Eqs. (37″) and (38′) are given, along with the corresponding zero-point energies, in Tables VII and VIII. The theoretical electron affinities $\mathrm{EA}_{\mathrm{ind}}$, $\mathrm{EA}_{\mathrm{ind+ec+}m\mathrm{dis}}$ and $\mathrm{EA}_{\mathrm{ind+ec+}m\mathrm{dis+at}}$ are given in Tables IX and X. The deviations of the theoretical EAs from the experimental values are shown in Figs. 15 and 16.

It is important to note that the many-body terms V_{ind}, V_{ec}, $V_{m\mathrm{dis}}$ and $V_{\mathrm{at}}^{\mathrm{anion}}$ all depend on the *absolute* values of the $Ar–X^-$ distances. Therefore, we must consider the uncertainties in these terms due to the absolute uncertainty in R_m in the pair potentials, which, as mentioned in Sec. IV A, is ± 0.2 Å for both $ArBr^-$ and Ar^-. In order to estimate the uncertainties in the many-body terms, we calculated the changes in these terms in the Ar_2Br^- and Ar_2I^- systems with the Ar–Ar distance fixed at the Ar_2 equilibrium value, as the $Ar–X^-$ distances were varied over ± 0.2 Å about the ArX^- equilibrium values. To estimate these uncertainties in the larger clusters, the Ar_2X^- uncertainties were multiplied by the number of nearest neighbor Ar–Ar pairs in contact with

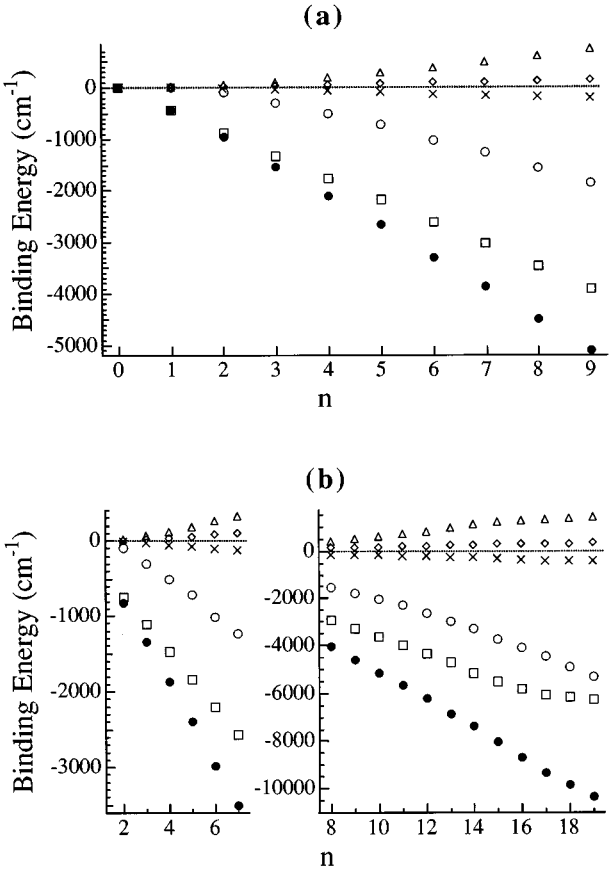

FIG. 14. Calculated contributions to the binding energies of (a) Ar_nBr^- and (b) Ar_nI^- anions. Solid circles: total BE. Open squares: Ar–Br^- contribution. Open circles: Ar–Ar contribution. Open triangles: nonadditive induction. Crosses: exchange charge and multipole dispersion. Open diamonds: triple-dipole dispersion.

the halide. The uncertainties introduced into the calculated EAs were found to be significantly larger than those due to the uncertainty in $\epsilon_a - \epsilon_X$ in the pair potentials. These uncertainties are displayed as error bars in Figs. 15 and 16.

TABLE VII. Calculated Ar_nBr^- anion and Ar_nBr neutral X state binding energies and zero point energies, including nonadditive terms. IND: nonadditive induction. EC: exchange charge. MDIS: dispersion multipole. AT: Axilrod–Teller triple-dipole dispersion. Energies are in cm^{-1}.

	IND		IND+EC+MDIS		IND+EC+MDIS+ AT (anion)		AT (neutral)	
n	ϵ_a	ω_0^a	ϵ_a	ω_0^a	ϵ_a	ω_0^a	ϵ_X	ω_0^X
1	438.8	20.7	438.8	20.7	438.8	20.7	133.1	15.6
2	942.4	53.7	955.9	56.1	946.8	55.0	343.7	41.7
3	1515.3	98.5	1555.7	105.1	1528.9	102.3	646.1	83.3
4	2081.3	142.6	2148.4	153.2	2103.9	148.8	950.0	124.7
5	2640.9	185.0	2734.3	199.0	2672.3	193.5	1255.5	164.7
6	3273.3	236.7	3402.4	255.2	3315.3	247.6	1643.6	207.8
7	3819.9	278.3	3974.4	300.4	3871.5	291.8	1978.7	262.0
8	4434.4	326.4	4620.2	351.6	4494.4	341.1	2385.1	307.4
9	5029.0	367.2	5238.7	395.2	5091.0	381.9	2783.7	349.6

TABLE VIII. Calculated Ar_nI^- anion and Ar_nI neutral X state binding energies and zero point energies, including nonadditive terms. IND: nonadditive induction. EC: exchange charge. MDIS: dispersion multipole. AT: Axilrod–Teller triple-dipole dispersion. Energies are in cm^{-1}.

	IND		IND+EC+MDIS		IND+EC+MDIS +AT (anion)		AT (neutral)	
n	ϵ_a	ω_0^a	ϵ_a	ω_0^a	ϵ_a	ω_0^a	ϵ_X	ω_0^X
1	369.4	17.3	369.4	17.3	369.4	17.3	151.6	14.6
2	814.6	48.4	825.2	50.4	817.0	49.2	379.0	40.6
3	1338.4	90.2	1369.9	96.0	1345.7	92.6	699.7	81.4
4	1859.9	132.3	1912.3	141.5	1871.5	136.4	1020.8	122.1
5	2378.0	171.8	2451.2	184.0	2393.7	177.7	1342.6	161.6
6	2967.4	221.9	3066.3	239.4	2985.9	229.2	1740.5	203.9
7	3476.4	261.5	3595.8	280.9	3499.6	270.5	2080.2	251.2
8	4040.0	306.9	4179.8	330.7	4062.8	316.2	2482.0	292.6
9	4567.5	344.5	4721.2	366.2	4585.0	352.0	2859.1	325.1
10	5102.2	386.5	5285.1	415.0	5131.7	398.9	3246.9	378.1
11	5623.9	423.4	5821.0	456.8	5647.2	436.2	3627.1	415.7
12	6197.5	475.9	6427.8	510.4	6233.0	488.9	4047.9	470.3
13	6818.0	516.8	7068.8	554.8	6847.5	528.7	4533.9	513.4
14	7363.8	547.9	7625.0	593.4	7371.8	557.4	4957.0	554.8
15	8021.4	610.6	8322.8	649.3	8038.4	617.9	5465.2	619.4
16	8615.8	683.1	8973.2	725.1	8673.8	694.6	5908.9	667.5
17	9232.3	763.9	9647.9	808.9	9336.7	781.2	6361.9	747.4
18	9737.0	818.1	1 0159.9	864.8	9840.0	836.3	6810.4	802.8
19	1 0247.0	872.0	1 0676.5	921.2	1 0347.4	891.3	7254.8	855.9

The addition of the many-body induction term significantly decreases the EA compared with the additive calculation. [Compare Figs. 15(a) and 16(a) with Figs. 10 and 11.] EA_{ind} is closer to the experimental values than EA_{add}, but is somewhat overcorrected. This is clearest in the Ar_nI clusters, in which EA_{ind} lies well below the experimental uncertainty region (shaded areas in Figs. 15 and 16) for $n=6$, 7 and 9–19. Thus, the Ar_nI results clearly indicate the need for additional nonadditive terms. In the Ar_nBr clusters, the experimental and theoretical EA uncertainty regions overlap except for $n=8$ and 9, but the EA_{ind} values are all systematically lower than the experimental EAs, again suggesting that induction effects alone decrease the electron affinity by too much.

TABLE IX. Ar_nBr electron affinities calculated with various non-additive terms. EA_{ind} nonadditive induction term only. $EA_{ind+ec+mdis}$ nonadditive induction, exchange charge, and multipole dispersion terms. $EA_{ind+ec+mdis+at}$: induction, exchange charge, multipole dispersion, and triple-dipole dispersion terms. Energies are in cm^{-1}.

n	EA_{ind}	$EA_{ind+ec+mdis}$	$EA_{ind+ec+mdis+at}$
0	27 129.2	27 129.2	27 129.2
1	27 429.8	27 429.8	27 429.8
2	27 710.8	27 721.9	27 718.9
3	27 968.5	28 002.2	27 993.0
4	28 218	28 275	28 259
5	28 460	28 540	28 517
6	28 681	28 792	28 761
7	28 897	29 029	28 992
8	29 088	29 249	29 205
9	29 271	29 453	29 404

TABLE X. Ar_nI electron affinities calculated with various non-additive terms. EA_{ind}: nonadditive induction term only. $EA_{ind+ec+mdis}$: nonadditive induction, exchange charge, and multipole dispersion terms. $EA_{ind+ec+mdis+at}$: induction, exchange charge, multipole dispersion, and triple-dipole dispersion terms. Energies are in cm^{-1}.

n	EA_{ind}	$EA_{ind+ec+mdis}$	$EA_{ind+ec+mdis+at}$
0	24 673.3	24 673.3	24 673.3
1	24 888.3	24 888.3	24 888.3
2	25 095.4	25 103.9	25 102.6
3	25 286.6	25 312.3	25 308.1
4	25 474	25 518	25 510
5	25 660	25 721	25 708
6	25 828	25 909	25 893
7	25 995	56 095	26 073
8	26 138	26 254	26 231
9	26 268	2 6400	26 372
10	26 410	26 565	26 537
11	26 537	26 701	26 673
12	26 680	26 875	26 840
13	26 798	27 011	26 972
14	26 903	27 119	27 086
15	27 039	27 302	27 248
16	27 156	27 472	27 411
17	27 323	27 693	27 614
18	27 336	27 712	27 669
19	27 431	27 811	27 731

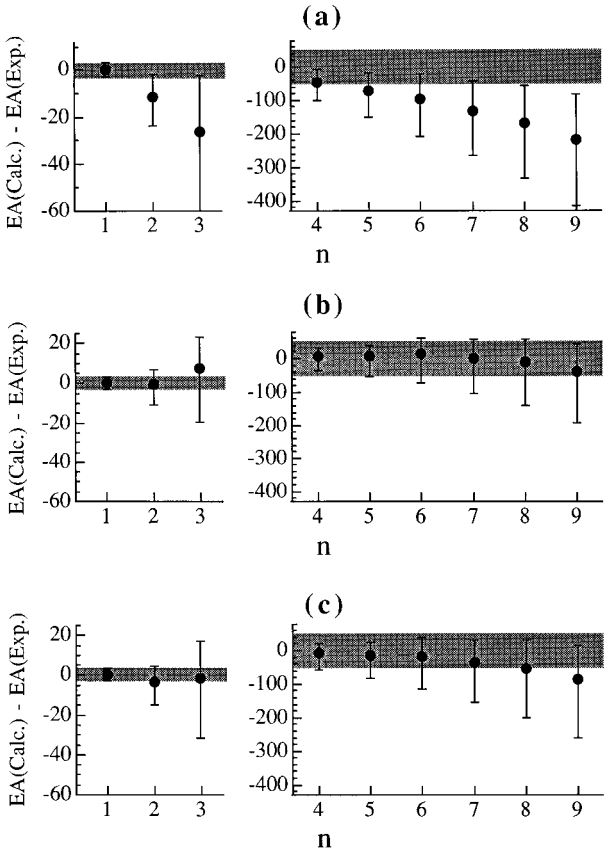

FIG. 15. Differences between calculated and experimental EAs for Ar_nBr, plotted as a function of n, including various three-body terms: (a) $EA_{ind}-EA_{expt}$, (b) $EA_{ind+ec+mdis} - EA_{expt}$, (c) $EA_{ind+ec+mdis+at} - EA_{expt}$. The shaded region represents the experimental uncertainty. The error bars represent the uncertainty in the calculated EAs.

Inclusion of V_{ec} and V_{mdis} in the calculation brings the theoretical EAs closer to the experimental results. [See Figs. 15(b) and 16(b).] In the case of Ar_nBr, $EA_{ind+ec+mdis}$ lies within the experimental error bars in all cases except for Ar_3Br, which is overcorrected by about 9 cm^{-1}. But even in this case, the model potential and experimental uncertainty regions overlap. For the Ar_nI clusters, $EA_{ind+ec+mdis}$ is overcorrected by 3.8–20.1 cm^{-1} for $n=2$–5, which is outside the experimental error bars (the shaded region in Figs. 15 and 16). For $6\leqslant n\leqslant 19$, $EA_{ind+ec+mdis}$ lies within experimental uncertainties except for $n=13$–15 and $n=17$. However, as in the Ar_nBr clusters, the theoretical and experimental uncertainty ranges overlap in all cases for Ar_nI.

Inclusion of the Axilrod–Teller term brings the theoretical EAs closer to experiment for the smaller clusters, but overcorrects somewhat for some of the larger clusters. [See Figs. 15(c) and 16(c)]. Now for the Ar_nBr clusters $EA_{ind+ec+mdis+at}$ lies within the experimental uncertainties for all cases except $n=9$. For $Ar_{2-4}I$ addition of the Axilrod–Teller term brings the theoretical EA closer to the experimental result, but is still a few wavenumbers above the experimental error bars. For $n=5$–10, 17, and 18, the theoretical result is within experimental uncertainties, but lies below the uncertainty region for $n=11$–16 and 19. But, again, the theoretical and experimental error bars overlap in all cases. Thus, inclusion of the triple-dipole term appears to help somewhat for the smaller clusters, but, because of the uncertainties in V_{ind} and $V_{ec}+V_{mdis}$ it is not possible to draw definite conclusions about the importance of the Axilrod–Teller term from the present results. To do so would require more precise knowledge of R_m in the pair potentials.

V. CONCLUSIONS

We have obtained experimental electron affinities and electronic structure information from the ZEKE and PDTP spectra of $Ar_{2-9}Br^-$ and $Ar_{2-9}I^-$. We have compared these with electronic state splittings and EAs calculated from both pairwise additive and nonadditive model potentials. The following conclusions can be drawn from this work.

(1) The first-order degenerate perturbation theory treatment of the open-shell neutral potentials described in Sec. IV E is accurate enough to account for the $X-I$ electronic state splittings observed in $Ar_{2-3}Br$ and $Ar_{2-7}I$, within experimental uncertainties. (See Fig. 8). However, this model somewhat overestimates the $X-II$ state splittings for $Ar_{2-3}Br$ and $Ar_{2-3}I$, possibly indicating that the spin–orbit splitting decreases as Ar atoms are added around the halogen. (See Fig. 9.)

(2) A pairwise additive model of the anion potentials is completely inadequate to account for the experimentally measured EAs. (See Figs. 10 and 11.) Nonadditive effects in the anion are clearly very important.

(3) The many-body induction effect is the most important nonadditive effect in the anion potential. Inclusion of V_{ind} accounts for most of the discrepancy between the addi-

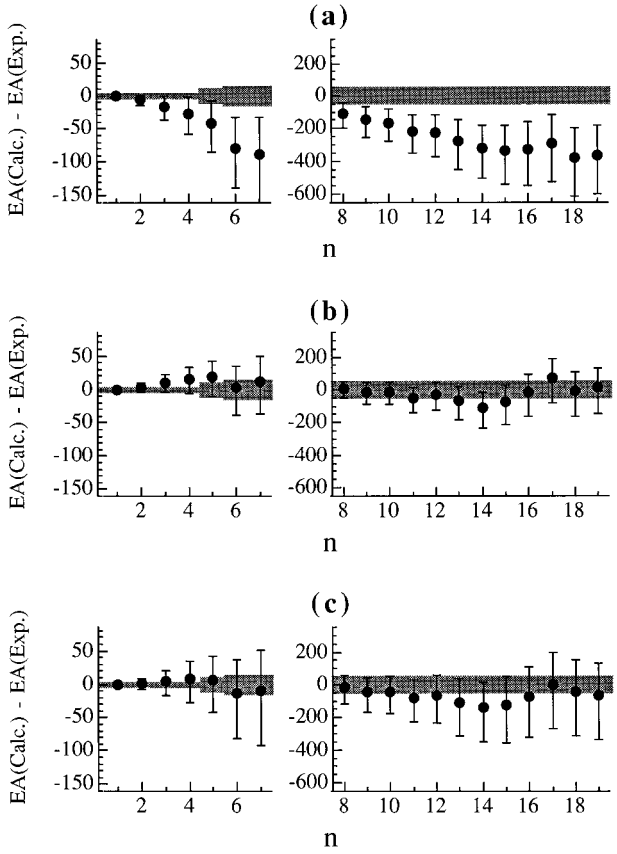

FIG. 16. Differences between calculated and experimental EAs for Ar_nI, plotted as a function of n, including various three-body terms: (a) $EA_{ind}-EA_{expt}$, (b) $EA_{ind+ec+mdis}-EA_{expt}$, (c) $EA_{ind+ec+mdis+at}-EA_{expt}$. The shaded region represents the experimental uncertainty. The error bars represent the uncertainty in the calculated EAs.

tive and experimental EAs, but somewhat overcorrects, especially in the case of Ar_nI. This result is consistent with the work of Berkowitz and others[18] who found a nonadditive inductive effect to be very important to model the experimental BEs of $Br^-(H_2O)_n$ clusters. We also note that, although not explicitly discussed by Bowen and coworkers in their paper on Ar_nO^- clusters,[16] it seems likely that the nonadditive induction effect may in large part account for the nonlinearity of the binding energies as a function of n observed by them for $n<12$. (See Fig. 4 of Ref. 16.)

(4) The exchange/dispersion multipole term also plays an important role. In both the $Ar_{2-9}Br^-$ and $Ar_{2-19}I^-$ clusters inclusion of the V_{ec} and V_{mdis} terms in the EA calculation brings the calculated EAs within the experimental error bars, when the uncertainty in the size of the induction effect due to the uncertainty of the pair potential bond length is taken into account.

(5) Inclusion of the triple-dipole dispersion effect in the anion and neutral potentials appears to slightly improve the agreement with experiment for the smaller clusters ($Ar_{2-5}Br^-$ and $Ar_{2-5}I^-$), but makes the fit slightly worse for the larger clusters. However, due to the uncertainties in R_m in the $Ar-X^-$ pair potentials, nothing conclusive can be said about the role of the triple-dipole dispersion effect in these clusters on the basis of our results. Furthermore, we cannot draw any conclusions about the role of three-body exchange effects or higher-order multipole dispersion terms from the present work.

Overall, this type of detailed energetic study of many-body effects is complementary to studies of nonadditive effects via high resolution spectroscopy. In this type of experiment we are able to directly measure the difference between anion and neutral binding energies, allowing a direct comparison of experimental observables with model potentials including nonadditive effects. However, due to limited resolution and uncertainties in the pair potentials this experiment is not sensitive to the most subtle nonadditive effects, such as the triple-dipole dispersion energy. This is in contrast to the high resolution spectroscopic studies of the Ar_2-HX systems,[3,7–10] which provide precise values of molecular constants. Comparison of such results with nonadditive model potentials is more difficult, but can in principle provide more precise information on nonadditive effects.

Further theoretical work needs to be done to interpret the vibrational structure observed in the smaller clusters ($Ar_{2-3}Br^-$ and $Ar_{2-3}I^-$) studied here. These spectra present an opportunity to test the various methods of dynamical calculations that have been developed for weakly bound clusters,[75] and such studies would be welcome.

In the future, we hope to observe the ZEKE spectrum of Ar_2Cl^-. This would allow direct comparison with the recently published *ab initio* study of this system by Burcl *et al.*[68] Also, the Ar_2Cl neutral cluster would present a more tractable problem for *ab initio* theorists than the larger halogen containing clusters studied in the present work.

ACKNOWLEDGMENTS

This research is supported by the Air Force Office of Scientific Research under Contract No. F49620-94-1-0115, and by a Department of Defense Augmentation Award for Science and Engineering Research Training under Contract No. F49620-94-1-0412. The authors also wish to thank R. B. Gerber, P. Jungwirth, A. Krylov, C. C. Martens, and Z. Li for helpful discussions and for providing molecular dynamics programs. D. M. Neumark is a Camille and Henry Dreyfus Teacher–Scholar.

[1] H. Margenau and N. R. Kestner, *Theory of Intermolecular Forces* (Pergamon, Oxford, 1969), Chap. 5.
[2] W. J. Meath and R. A. Aziz, Mol. Phys. **52**, 225 (1984).
[3] M. J. Elrod and R. J. Saykally, Chem. Rev. **94**, 1975 (1994), and references therein.
[4] Y. Zhao, I. Yourshaw, G. Reiser, C. C. Arnold, and D. M. Neumark, J. Chem. Phys. **101**, 6538 (1994).
[5] Y. Zhao, C. C. Arnold, and D. M. Neumark, J. Chem. Soc. Faraday Trans. **89**, 1449 (1993).
[6] Y. Xu, W. Jäger, and M. C. L. Gerry, J. Chem. Phys. **100**, 4171 (1994).
[7] M. A. Suhm and D. J. Nesbitt, Chem. Soc. Rev. **24**, 45 (1995); A. McIlroy, R. Lascola, C. M. Lovejoy, and D. J. Nesbitt, J. Phys. Chem. **95**, 2636 (1991).
[8] M. J. Elrod, J. G. Loeser, and R. J. Saykally, J. Chem. Phys. **98**, 5352 (1993).
[9] M. M. Szczesniak, G. Chalasinski, and P. Piecuch, J. Chem. Phys. **99**, 6732 (1993); S. M. Cybulski, M. M. Szczesniak, and G. Chalasinski, *ibid.* **101**, 10708 (1994).

[10] (a) A. R. Cooper and J. M. Hutson, J. Chem. Phys. **98**, 5337 (1992); (b) M. J. Elrod, R. J. Saykally, A. R. Cooper, and J. M. Hutson, Mol. Phys. **81**, 579 (1994); (c) A. Ernesti and J. M. Hutson, Phys. Rev. A **51**, 239 (1995).
[11] S. Martrenchard-Barra, C. Jouvet, C. Lardeux-Dedonder, and D. Solgadi, J. Chem. Phys. **98**, 5281 (1993).
[12] J. P. Visticot, P. de Pujo, J. M. Méstdagh, A. Lallement, J. Berlande, O. Sublemontier, P. Meynadier, and J. Cuvellier, J. Chem. Phys. **100**, 158 (1994).
[13] (a) C. R. Bieler, D. D. Evard, and K. C. Janda, J. Phys. Chem. **94**, 7452 (1990); (b) D. G. Jahn, S. G. Clement, and K. C. Janda, J. Chem. Phys. **101**, 283 (1994).
[14] T. Bürgi, T. Droz, and S. Leutwyler, Chem. Phys. Lett. **225**, 351 (1994).
[15] G. Markovich, S. Pollack, R. Giniger, and O. Cheshnovsky, J. Chem. Phys. **101**, 9344 (1994).
[16] S. T. Arnold, J. H. Hendricks, and K. H. Bowen, J. Chem. Phys. **102**, 39 (1995).
[17] D. W. Arnold, S. E. Bradforth, E. H. Kim, and D. M. Neumark, J. Chem. Phys. **102**, 3510 (1995); **97**, 9468 (1992).
[18] L. S. Sremaniak, L. Perera, and M. L. Berkowitz, Chem. Phys. Lett. **218**, 377 (1994).
[19] K. Müller-Dethlefs, M. Sander, and E. W. Schlag, Z. Naturforsch. Teil A **39**, 1089 (1984); Chem. Phys. Lett. **12**, 291 (1984); K. Müller-Dethlefs, and E. W. Schlag, Annu. Rev. Phys. Chem. **42**, 109 (1991).
[20] (a) T. N. Kitsopoulos, I. M. Waller, J. G. Loeser, and D. M. Neumark, Chem. Phys. Lett. **159**, 300 (1989); (b) C. J. Chick, Y. Zhao, T. N. Kitsopoulos, and D. M. Neumark, J. Chem. Phys. **97**, 6121 (1992); (c) T. N. Kitsopoulos, Ph.D. thesis, University of California, Berkeley, 1991; (d) C. C. Arnold, Ph.D. thesis, University of California, Berkeley, 1994.
[21] J. M. B. Bakker, J. Phys. E **6**, 785 (1973).
[22] T. Baer, W. B. Peatman, and E. W. Schlag, Chem. Phys. Lett. **4**, 243 (1969); R. Spohr, P. M. Guyon, W. A. Chupka, and J. Berkowitz, Rev. Sci. Instrum. **42**, 1872 (1971).
[23] C. E. Moore, *Atomic Energy Levels*, Vol. I, Circ. Natl. Bur. Std. 467 (1949).
[24] H. Haberland, Z. Phys A **307**, 35 (1982).
[25] C. Blondel, P. Cacciani, C. Delsart, and R. Trainham, Phys. Rev. A **40**, 3698 (1989).
[26] H. Hotop and W. C. Lineberger, J. Phys. Chem. Ref. Data **14**, 731 (1985).
[27] P. Casavecchia, G. He, R. K. Sparks, and Y. T. Lee, J. Chem. Phys. **75**, 710 (1981).
[28] (a) G. Liuti, and F. Pirani, Chem. Phys. Lett. **122**, 245 (1985); (b) D. Cappelletti, G. Liuti, and F. Pirani, *ibid*. **183**, 297 (1991); (c) R. Cambi, D. Cappelletti, G. Liuti, and F. Pirani, J. Chem. Phys. **95**, 1852 (1991).
[29] R. A. Aziz, and M. J. Slaman, Mol. Phys. **58**, 679 (1986). A more accurate Ar–Ar potential has recently been published—the HFDID 1 potential of Aziz, which was fit to more recent spectroscopic data [R. A. Aziz, J. Chem. Phys. **99**, 4518 (1993)]. However, it was felt that the simpler HFD-B2 potential is sufficiently accurate for the purposes of this work.
[30] Z. Li, A. Borrmann, and C. C. Martens, J. Chem. Phys. **97**, 7234 (1992); A. Borrmann, Z. Li, and C. C. Martens, *ibid.* **98**, 8514 (1993).
[31] M. P. Allen, and D. J. Tildesley, *Computer Simulation of Liquids* (Oxford University, Oxford, 1987), p. 231.
[32] P. R. Bevington, *Data Reduction and Error Analysis for the Physical Sciences* (McGraw-Hill, New York, 1969), Chap. 11.
[33] E. B. Wilson, J. C. Decius, and P. C. Cross, *Molecular Vibrations* (Dover, New York, 1955).
[34] D. O. Harris, G. G. Engerholm, and W. D. Gwinn, J. Chem. Phys. **43**, 1515 (1965).
[35] J. C. Light, I. P. Hamilton, and J. V. Lill, J. Chem. Phys. **82**, 1400 (1985).
[36] R. B. Metz, Ph.D. thesis, University of California, Berkeley, 1991.
[37] W. G. Lawrence and V. A. Apkarian, J. Chem. Phys. **101**, 1820 (1994). Note the misprint in Eq. (A1) of this paper. The matrix element $\langle \frac{1}{2},-\frac{1}{2}|H'|\frac{3}{2},\frac{1}{2}\rangle$ should read $\frac{1}{3}V_{01}-\frac{2}{3}V_{-10}$, in the notation of this reference.
[38] V. Aquilanti, G. Liuti, F. Pirani, and F. Vecchiocattivi, J. Chem. Soc. Faraday Trans. **85**, 955 (1989).
[39] W. E. Baylis, J. Phys. B **10**, L477 (1977).
[40] D. L. Huestis and N. E. Schlotter, J. Chem. Phys. **69**, 3100 (1978).
[41] F. O. Ellison, J. Am. Chem. Soc. **85**, 3540 (1963); J. C. Tully, J. Chem. Phys. **58**, 1396 (1973).
[42] (a) K. M. Sando, G. J. Erickson, and R. C. Binning Jr., J. Phys. B **12**, 2697 (1979); (b) G. J. Erickson, and K. M. Sando, Phys. Rev. A **22**, 1500 (1980).
[43] L. C. Balling and J. J. Wright, J. Chem. Phys. **79**, 2941 (1983).
[44] J. A. Boatz and M. E. Fajardo, J. Chem. Phys. **101**, 3472 (1994).
[45] (a) A. I. Krylov, R. B. Gerber, and V. A. Apkarian, Chem. Phys. **189**, 261 (1994); (b) A. I. Krylov, and R. B. Gerber, Chem. Phys. Lett. **231**, 395 (1994).
[46] B. M. Axilrod and E. Teller, J. Chem. Phys. **11**, 299 (1943); B. M. Axilrod, *ibid*. **19**, 719 (1951).
[47] Y. Muto, Proc. Phys.-Math. Soc. Jpn. **17**, 629 (1943).
[48] (a) K. T. Tang, J. M. Norbeck, and P. R. Certain, J. Chem. Phys. **64**, 3063 (1976); (b) D. J. Margoliash, T. R. Proctor, G. D. Zeiss, and W. J. Meath, Mol. Phys. **35**, 747 (1978); (c) A. Kumar and W. J. Meath, Mol. Phys. **54**, 823 (1985).
[49] G. Chalasinski, M. M. Szczesniak, and S. M. Cybulski, J. Chem. Phys. **92**, 2481 (1990).
[50] (a) A. D. Koutselos and E. A. Mason, J. Chem. Phys. **85**, 2159 (1986); (b) H. L. Kramer, and D. R. Herschbach, J. Chem. Phys. **53**, 2792 (1970); (c) K. T. Tang, Phys. Rev. **177**, 108 (1969).
[51] J. C. Slater and J. G. Kirkwood, Phys. Rev. **37**, 682 (1931); K. S. Pitzer, Adv. Chem. Phys. **2**, 59 (1959); J. N. Wilson, J. Chem. Phys. **43**, 2564 (1965).
[52] R. J. Bell, J. Phys. B **3**, 751 (1970).
[53] F. J. Vesely, J. Comput. Phys. **24**, 361 (1977).
[54] E. L. Pollock and B. J. Alder, Phys. Rev. Lett. **41**, 903 (1978).
[55] P. Stampfli, J. Chem. Phys. **101**, 6024 (1994).
[56] For example, water: (a) F. H. Stillinger and C. W. David, J. Chem. Phys. **69**, 1473 (1978); (b) P. Barnes, J. L. Finney, J. D. Nicholas, and J. E. Quinn, Nature **282**, 459 (1979); (c) P. Ahlström, A. Wallqvist, S. Engström, and B. Jönsson, Mol. Phys. **68**, 563 (1989); (d) J. Caldwell, L. X. Dang, and P. A. Kollman, J. Am. Chem. Soc. **112**, 9144 (1990); acetone: (e) P. Jedlovszky and G. Pálinkás, Mol. Phys. **84**, 217 (1995).
[57] For example, (a) Xe_n^{2+}: J. G. Gay and B. J. Berne, Phys. Rev. Lett. **49**, 194 (1982); (b) $Na^+(H_2O)_n$: P. Perez, W. K. Lee, and E. W. Prohofsky, J. Chem. Phys. **79**, 388 (1983); (c) $X(H_2O)_n$ (K=halide and alkali ions): S. Sung and P. C. Jordan, *ibid*. **85**, 4045 (1986); (d) $X_nBr_2^+$ (X=Ar, CO_2): L. Perera and F. G. Amar, *ibid*. **90**, 7354 (1989); (e) $(H_2O)_nX$ (X=Na^+, Cl^-): L. Perera, and M. L. Berkowitz, *ibid*. **95**, 1954 (1991); **99**, 4236 (1993).
[58] The contribution of the term in B to the induced quadropole moment is estimated to be approximately 20% of the C contribution, and of opposite sign, where we have used the values of B for Ar from Ref. 74.
[59] U. C. Dikshit and M. Kumar, Phys. Status Solidi B **165**, 599 (1991).
[60] A. D. Buckingham, Adv. Chem. Phys. **12**, 107 (1967).
[61] C. J. F. Böttcher, *Theory of Electric Polarization*, 2nd ed. (Elsevier, Amsterdam, 1973), Vol. I.
[62] J. Applequist, Chem. Phys. **85**, 279 (1984); **190**, 153 (1995).
[63] R. L. Asher, D. A. Micha, and P. J. Brucat, J. Chem. Phys. **96**, 7683 (1992).
[64] B. G. Dick, Jr. and A. W. Overhauser, Phys. Rev. **112**, 90 (1958).
[65] L. Jansen, Adv. Quantum Chem. **2**, 119 (1965).
[66] A. J. Lacey and W. Byers Brown, Mol. Phys. **27**, 1013 (1974).
[67] (a) M. M. Szczesniak, G. Chalasinski, and P. Piecuch, J. Chem. Phys. **99**, 6732 (1993); (a) S. M. Cybulski, M. M. Szczesniak, and G. Chalasinski, J. Chem. Phys. **101**, 10708 (1994).
[68] R. Burcl, S. M. Cybulski, M. M. Szczesniak, and G. Chalasinski, J. Chem. Phys. **103**, 299 (1995).
[69] B. Guillot, R. D. Mountain, and G. Bimbaum, Mol. Phys. **64**, 747 (1988).
[70] W. Kolos and A. Les, Int. J. Quantum Chem. **6**, 1101 (1972).
[71] R. J. Wheatley, Mol, Phys. **79**, 597 (1993); J. Comput. Chem. **15**, 1187 (1994).
[72] W. H. Press, S. A. Teukolsky, W. T. Vetterling, and B. P. Flannery, *Numerical Recipes*, 2nd ed. (Cambridge University Press, Cambridge, 1992), p. 213.
[73] K. L. C. Hunt, Chem. Phys. Lett. **70**, 336 (1980).
[74] G. Maroulis and D. M. Bishop, J. Phys. B **18**, 4675 (1985).
[75] See, for example, (a) the vibrational SCF method: T. R. Horn, R. B. Gerber, and M. A. Ratner, J. Chem. Phys. **91**, 1813 (1989); T. R. Horn, R. B. Gerber, J. J. Valentini, and M. A. Ratner, *ibid*. **94**, 6728 (1991), (b) DVR method: R. M. Whitnell and J. C. Light, *ibid*. **90**, 1774 (1989); D. M. Leitner, J. D. Doll, and R. M. Whitnell, *ibid*. **94**, 6644 (1991), (c) basis set expansion methods: A. R. Cooper, S. Jain, and J. M. Hutson, *ibid*. **98**, 2160 (1993).